Parametric analysis of the stability of a bicycle taking into account geometrical, mass and compliance properties

Alberto Doria

Department of Industrial Engineering

University of Padova

Via Venezia 1, 35131, Padova, Italy

e-mail: alberto.doria@unipd.it

*Corresponding author

Valerio Favaron

Department of Industrial Engineering

University of Padova

Via Venezia 1, 35131, Padova, Italy

e-mail: valeriofavaron90@gmail.com

Luca Taraborrelli

Department of Industrial Engineering

University of Padova

Via Venezia 1, 35131, Padova, Italy

e-mail: luca.taraborrelli@yahoo.it

Sergio Roa

Mechanical Engineering Department

Universidad de los Andes

Carrera 1 Este # 19A-40, Bogotá, Colombia

e-mail: sd.roa48@uniandes.edu.co

Abstract: Some studies of bicycle stability have applied the Whipple Carvallo Bicycle Model (WCBM), which describes the roll and steer behaviour of a bicycle, allowing analysis of its characteristics of stability and in particular self-stability. One of the limitations of this model is that all structural elements are assumed to be rigid bodies. In this paper, the WCBM is extended to include the effect of front assembly lateral compliance, and analysis focuses on study of the open loop stability of a benchmark bicycle. Experimental tests to identify fork and wheel properties are presented and discussed. Stability analysis is carried out by a MATLAB numerical code, and specific stability indexes are calculated from plots of eigenvalues against speed. In order to rank the influence of design parameters on stability, numerical calculations are carried out in a full factorial experiment with two levels of eight design parameters. The results show that introducing front assembly compliance generates a wobble mode, but this has little effect on the range of self-stability. The forward displacement of the centre of mass of the rear frame and the increment in trail lead to large increments in the self-stability range, whereas increments in front wheel radius and wheelbase cause reduced stability.

Keywords: bicycle, stability, weave, capsize, wobble, front fork, wheel.

Biographical notes: Alberto Doria received the Laurea degree in Mechanical Engineering (with honors) from the University of Padova in 1984. In 1986 he joined the Italian Research Authority as contract researcher, becoming member of the design group of RFX, a fusion experiment funded by Euratom. He designed and developed the manipulator of the RFX machine. He received in 1987 the degree "Corso di Perfezionamento in Ingegneria del Plasma e della Fusione Termonucleare Controllata" from the University of Padova. In 1990 Alberto Doria joined the University of Padova as researcher of Mechanics of Machines. His research activity was in the fields of robotics and control of vibrations and noise. He developed particular Helmholtz resonators that were implemented in an air-conditioner. In 1997 Alberto Doria joined the Motorcycle Dynamics Research Group of Padova University. He begun a research activity in the field of two wheeled vehicles that included modeling, simulation and experimental issues. In 2002 Alberto Doria became Associate Professor of Mechanics of Machines at the University of Padova. The current research activities of Alberto Doria are: development of light vehicles for sustainable mobility; modal analysis and identification; vibration energy harvesting. In 2014 Alberto Doria has obtained the national qualification needed for becoming full professor. Alberto Doria is author of 110 scientific publications and has been responsible for research projects and contracts with companies. Alberto Doria is member of ASME.

Valerio Favaron achieved his master degree at the University of Padua in March 2015 with a thesis dealing with the effect of tyres inflation pressure on motorcycle stability, supervised by Professor Vittore Cossalter. Then, he was employed as a researcher at the Motorcycle Dynamics Research Group at the University of Padua. His field of expertise is related to the study of instability of two wheeled vehicle in particular referring to motorcycle weave and wobble.

Luca Taraborrelli graduated in Clinical Engineering in 2010 and he finished the Master's degree in Biomedical Engineering in 2012 at the University of Rome "La Sapienza". Successively, he achieved a Doctorate degree in Mechanical Engineering at the University of Padova with a thesis on

the “Identification and improvement of the dynamic properties of the components of two-wheeled vehicles”. In the framework of his PhD, he has been co-author of some publications in international journals and conference proceedings, collecting two “Best Paper Awards” at the ASME AVT 2014 and ASME AVT 2016 conferences. The research fields in which he is expert and passionate are biomechanics, mechanical vibrations and vehicle dynamics.

Sergio Roa earned a Master’s degree in Mechanical Engineering at Universidad de los Andes in Bogotá, Colombia. His Master’s studies were focused on four-wheel vehicle dynamics. Currently, he is pursuing a doctoral degree at Universidad de los Andes. Following the dynamics of two-wheel vehicles area, he is studying some aspects of performance in competitive road cycling. At this moment, he is doing an internship at University of Padova in Italy for studying the stability and vibrational comfort on cycling as part of the objectives in his doctoral studies.

---

1 Introduction

The development of modern bicycles, as carried out by cyclists and technicians, has mainly been achieved by a trial-and-error approach, although bicycle dynamics have attracted the attention of scientists and engineers since the late 19th century. The first realistic dynamic model of a bicycle suitable for studying stability characteristics was developed by Whipple and Carvallo (WCBM) in 1899 (Meijaard, 2007). It had three velocity degrees of freedom (DOF), and the model was based on three assumptions: that the rear frame and the rider form a single rigid body, the disc wheels roll without slipping and make point contact with the road surface, and all structural elements are rigid.

In recent years, the WCBM has been extended with new features (Schwab, 2012), (Doria, 2014), and new models including tyre properties (Doria 2013) have been developed (Klinger, 2014), (Bulsink, 2015). Studies and simulations of motorcycle dynamics (e.g., Cossalter, 2007) have also provided useful information for studying bicycles. However, although these studies and simulations are interesting, it is still difficult to identify the design parameters which have the greatest effect on stability in the various ranges of speed. The present work focuses on open loop stability and contributes to more knowledge of this topic.

The linear dynamics of a bicycle are mainly characterised by two modes of vibration (eigenvectors): capsize and weave. Capsize mode is dominated by roll rotation about an axis in the road plane which is instantaneously aligned with the rear frame of the bicycle. Weave mode is a combination of steer and roll rotations. Wobble (or shimmy) mode in bicycles, which mainly involves the front assembly, is generally significant only at high speeds (Klinger, 2014), (Magnani, 2013). The typical plots of the real and imaginary parts of the eigenvalues of bicycle modes against forward speed show two characteristic speeds: weave speed v_w (lowest speed at which weave mode is stable) and capsize speed v_c (highest speed at which capsize mode is stable). The range between v_w and v_c is the self-stability range. The speed range over which a bicycle is self-stable matches practical experience (Sharp 2008); self-stability is also related to rider-controlled stability (Kooijman 2011), (Åström 2005). For this reason, this work focuses on the effect of design parameters on the self-stability range.

Although a rigid bicycle is described by 25 parameters (Meijaard, 2007), a reduced set of these parameters is taken into account here; first, because preliminary analyses showed that some parameters have a negligible effect on stability, and second, because some parameters are functions of others (e.g., the mass and inertia properties of a wheel are functions of wheel radius). Stiffness parameters which define the compliance of the front assembly are also examined in the parametric analysis of stability, for both technical and methodological reasons. The geometry of the front assembly plays an important role in the stability and handling of two-wheeled vehicles (Cossalter, 2007), especially in steering into the fall phenomenon (Kooijman, 2011), so that the compliance of structural elements, which may alter nominal geometry (e.g., the attitude of the front wheel with respect to the road) may be important. As some recent studies (e.g., Klinger, 2014) include not only simple models of front assembly compliance, but also tyre models, it is sometimes difficult to understand the specific effect of compliance on the stability of capsize and weave modes.

In this study, the effects of selected design parameters on bicycle stability are analysed numerically according to a large series of simulations, planned following a method based on a full factorial experimental design (Montgomery, 2008). For each combination of design parameters, an eigenvalue plot is obtained and indexes representing the stability properties of the bicycle are derived. Correlation analysis between stability indexes and design parameters is then carried out.

The paper is organised as follows. The next section describes experimental analysis aimed at identifying the critical compliances of the front assembly (fork and wheel). Tests were carried out with the modal analysis approach and the stiffness values of components are given. In the third section, the WCBM is extended to include the effect of front assembly compliance, and a new 4-DOF bicycle model is developed and implemented in MATLAB. The fourth section describes parametric analysis of stability. A survey was first carried out to find relationships among the various design parameters. A set of independent parameters was found and realistic ranges of their variations were defined. Stability indexes and correlation analysis were then implemented in MATLAB. Lastly, numerical results are presented and discussed, and the design parameters are ranked in order of importance.

2 Identification of front assembly critical compliances

2.1 Methods

The components of the front assembly (fork and wheel) are mechanical systems with distributed mass, stiffness and damping properties. They were tested in the laboratory with the aim of identifying lumped stiffness properties suitable for implementation in an extended WCBM. This experimental approach was based on dynamic tests carried out with the modal analysis method (Ewins, 2000), since the stiffness properties exhibited by critical bicycle components in dynamic conditions are the most interesting from the viewpoint of stability analysis. Nevertheless, some static tests were also carried out for comparison and verification.

Testing forks and wheels when they are mounted on an actual bicycle is difficult, because rigid rotations about the steering axis, wheel spin axis and chassis deformation may interfere with measurements. The components were therefore tested in a configuration which can be reproduced in future experiments. In particular, the steerer tube of the fork was attached to a fixed structure with a

clamp (Fig. 1). The wheel hub was attached at both ends by a special fixture stiffly mounted on a massive base (Fig. 2). Wheel rotation was prevented by a strap. Some tests were also carried out with the wheel mounted on the fork, with the fork fixed to the stiff structure.

As the modal analysis approach required frequency response functions (FRFs) to be measured, the bicycle components were excited by a hammer for modal testing. Accelerations were measured in a mesh of testing points (14 for the fork, 8 for the wheel) by a tri-axial accelerometer which was moved each time to a different point of the mesh. To test the fork, the hammer impacts were applied in two directions perpendicular to the fork axis, so as to excite both lateral and longitudinal vibrations. The wheel was excited by hammer blows perpendicular to the wheel plane.

Experimental FRFs were calculated as the ratios between the cross-spectrum of the input signal (hammer force) and the output signal (acceleration) and the auto-spectrum of the input signal. For each point, the average of three measurements was examined. Natural frequencies, damping coefficients and modal shapes were identified by ModalVIEW, a software for modal analysis.

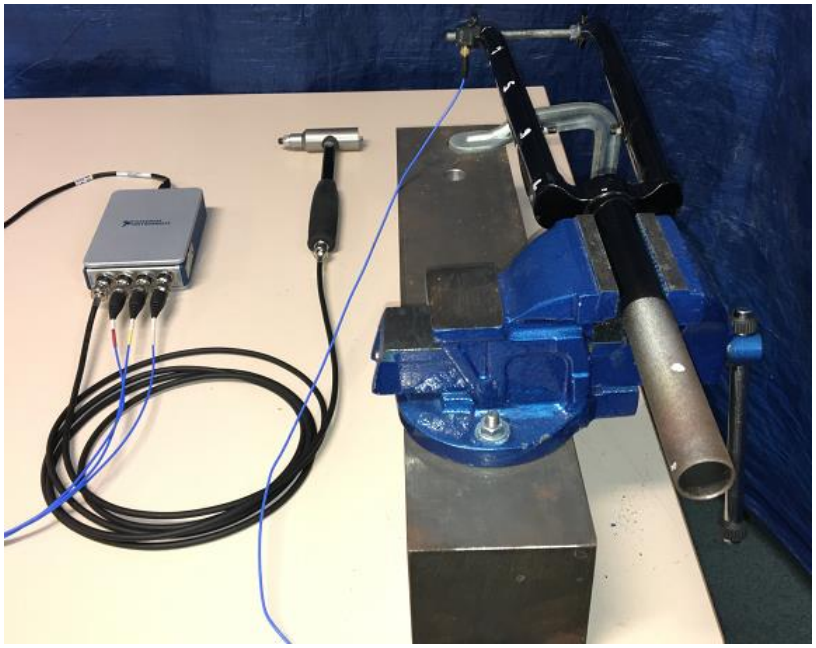

Figure 1. Front fork fixed in clamp.

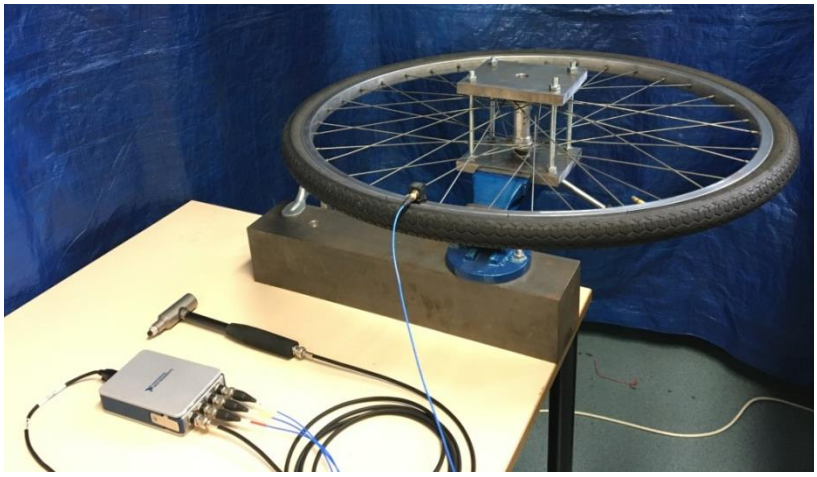

Figure 2. Wheel mounted with wheel hub attached at both ends.

2.2 Fork modes

In this study, an ordinary steel fork was tested with the modal analysis approach. Since the fork was tested without the wheel, a fake axle joining the fork-ends was added, to avoid unrealistic relative motions between the blades. The sizes of the fake axle and clamping elements were similar to those of a real bicycle.

Table 1 lists the test results, together with natural frequency f and viscous damping ζ (Ewins, 2000). The first vibration mode (Fig. 3) is lateral, dominated by the lateral bending of the two blades, which behave like two cantilever beams in parallel; the axle translates laterally and undergoes very little rotation. The whole behaves like a portal structure. The second mode of vibration is the longitudinal mode of the fork, dominated by longitudinal bending of the blades. The torsional mode takes place at high frequency and is characterised by rotation of the axle about the steer axis. It should be noted that a study carried out on a carbon fork and another steel fork (Doria, 2015) led to similar results, in both terms of natural frequencies and modal shapes.

Table 1. Modal properties of fork alone.

f (Hz)	ζ (%)	Description
73.94	1.31	Lateral bending
87.38	2.67	Longitudinal bending
196.3	0.391	Torsion

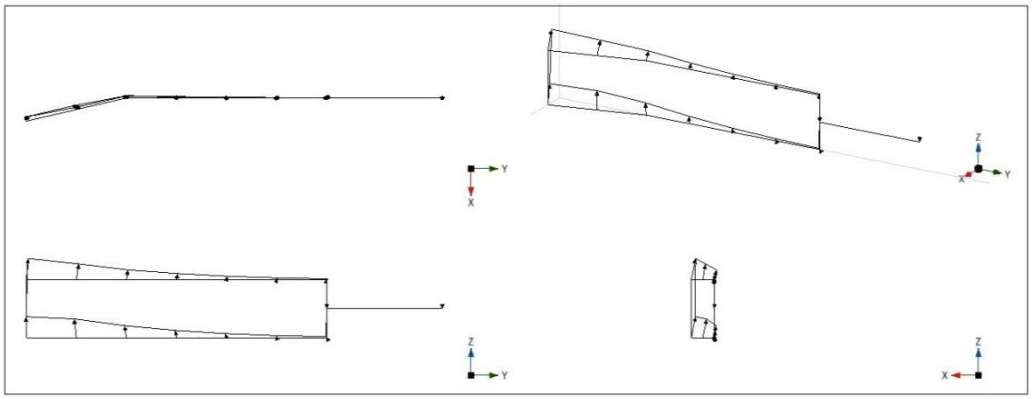

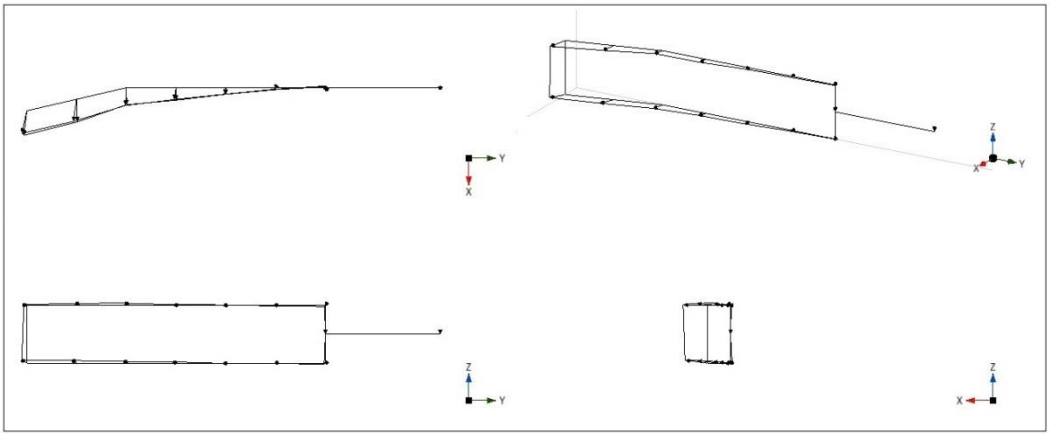

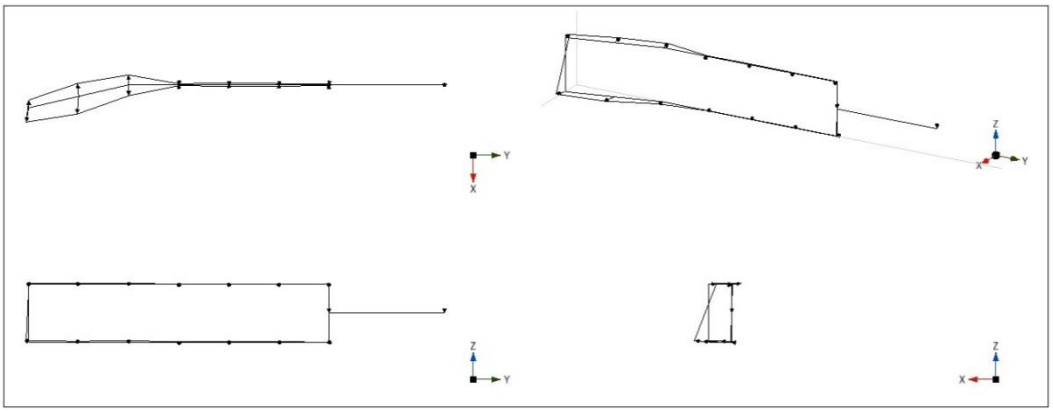

Figure 3. Modes of fork alone (from top: lateral, longitudinal and torsional modes).

2.3 Wheel modes

Some ordinary front wheels were also tested. The wheels were excited by hammer blows perpendicular to the wheel plane. Since measurements and modal properties turned out to be similar, results referring to only one wheel are listed in Table 2. Figure 4 shows that the first typical mode of the wheel is diametric, characterised by rigid rotation of the rim with the tyre about the diameter of the wheel. Since the hub is fixed and the rim is not deformed, this mode is dominated by spoke deformation. At higher frequencies, modes dominated by rim deformation appear. The first mode with rim deformation is C-shaped, in which out-of-plane deformation shows four nodes and four anti-nodes in the circumferential direction. The pair of anti-nodes along the same diameter are in phase with each other and in phase opposition with the pair of anti-nodes along the perpendicular diameter. At high frequency, an S-shaped mode appears, with six nodes and anti-nodes, and the adjacent points of the rim move in opposition. Higher-order modes could not be identified with only eight measurement points, owing to problems of spatial aliasing.

Table 2. Modal properties of wheel alone.

f (Hz)	ζ (%)	Description
27.75	1.607	Diametric
99.66	0.8707	C-shaped
148.8	1.292	S-shaped

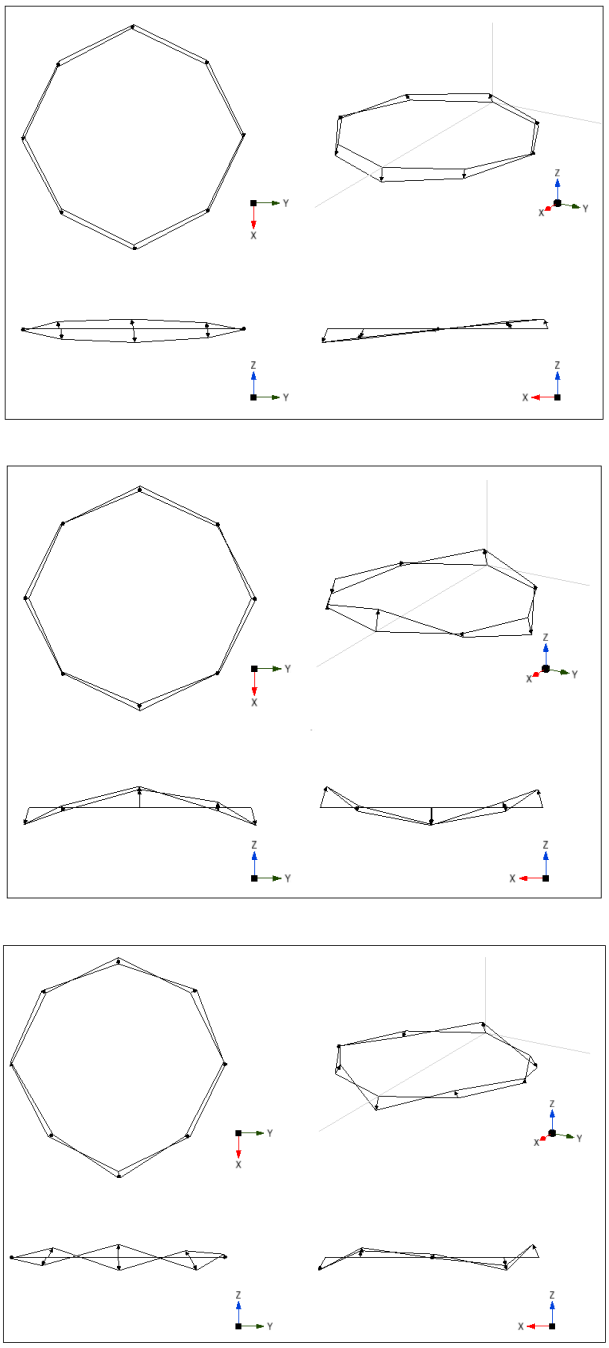

Figure 4. Modes of wheel alone (from top: diametric, C-shaped and S-shaped modes).

2.4 Front assembly modes

Modal analysis of the front assembly was carried out by testing the wheel and fork assembly. The results (Table 3) show that the first mode of the front assembly (17.7 Hz) is torsional, dominated by rotation of the front wheel about the diameter of the wheel, which is aligned with the steer axis. The modal shape (Fig. 5), shows that front fork deformability only plays a small role in this mode, as confirmed by the fact that the natural frequency of the torsion mode of the front assembly is much closer to that of the diametric mode of the wheel (27.75 Hz) than that of the torsional mode of the fork (196.3 Hz).

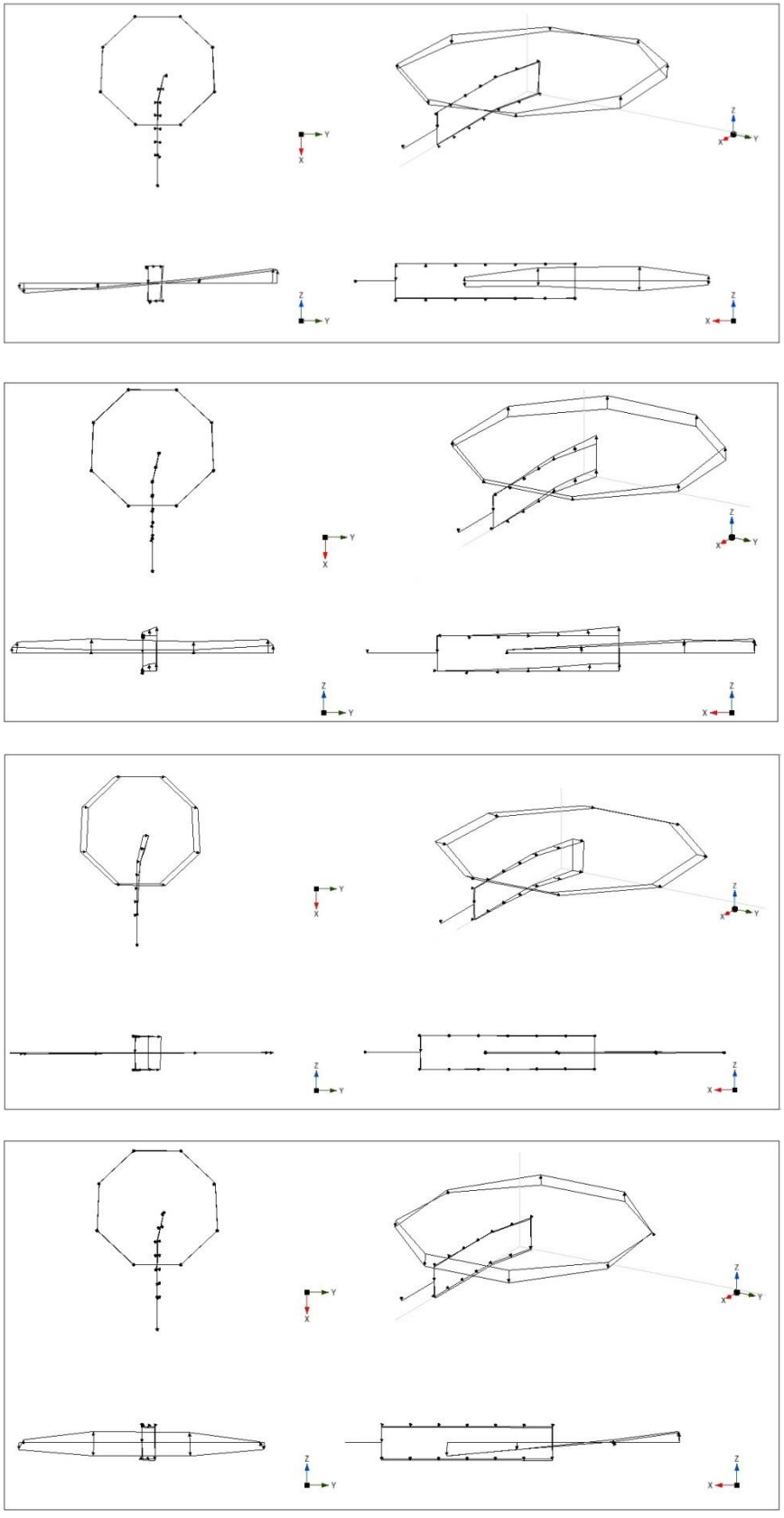

Figure 5. Modes of front assembly. From top: torsional, lateral, longitudinal and second lateral mode.

The second mode of the front assembly is lateral. This mode is the in-phase contribution of the lateral mode of the fork with the diametric mode of the wheel about the horizontal diameter. As the axle of the wheel moves almost parallel to itself, wheel rotation is mainly caused by wheel deformation. The natural frequency of this mode is closer to the natural frequency of the diametric mode of the wheel (27.75 Hz) than to that of the lateral mode of the fork (73.94 Hz).

The third mode is the longitudinal mode of the whole assembly: it is dominated by bending deformation of the fork longitudinally, with a natural frequency which is much lower than that of the longitudinal mode of the fork, owing to the considerable inertia of the wheel.

The fourth mode is the combination in phase opposition of the lateral mode of the fork with a diametric mode of the wheel; the deformation of the wheel dominates the modal shape. It should be noted that the natural frequency of this mode is higher than that of the lateral mode with in-phase vibrations of fork and wheel.

Table 3. Modal properties of fork with wheel.

f (Hz)	ζ (%)	Description
17.7	0.181	Torsional
24.99	0.552	Lateral bending
26.86	0.586	Longitudinal bending
53.38	1.041	Wheel diametric with fork in opposition

2.5 Identification of fork stiffness

This section identifies a lumped parameter model of the fork representing the behaviour of this component when the lateral mode is excited. Analysis of the lateral mode had shown that the blades of the fork behave like cantilever beams and that the rotation of the axle is less than the slopes at the ends of the blades, which allowed the model shown in Figure 6 to be developed.

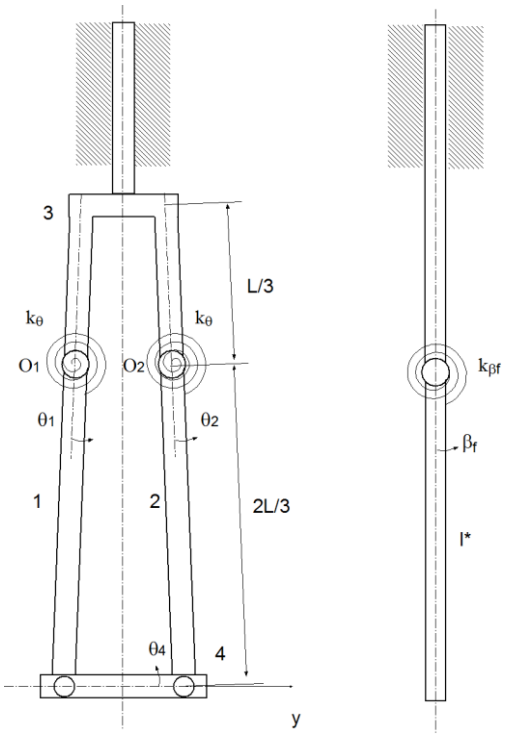

Figure 6. Fork model for lumped stiffness calculation.

The bending deformability of each blade (elements 1 and 2 in Fig. 6) is represented by introducing a revolute joint and a lumped rotational spring (stiffness k_θ) at location 1/3 L, in which L is the total span of the blade. This location matches the basic theory of elastic beams (Doria, 2016). The axle (element 4 in Fig. 6) is connected to the fork-ends by two revolute joints, so that the elements of the fork (blades, upper plate and axle) make up a four-bar linkage with two nearly parallel rockers. In this mechanism, the axle moves almost parallel to itself, matching the results of modal analysis. The four-bar linkage can be studied with the typical methods of mechanism analysis (Doughty, 1988).

The velocity ratios between the various links of the mechanism can be calculated from the velocity equations of the linkage. If rotation θ_1 of blade 1 is considered as the independent variable, the following velocity ratios can be calculated: $\tau_{21} = \dot{\theta}_2/\dot{\theta}_1$ (between the angular velocities of blade 2 and blade 1); $\tau_{41} = \dot{\theta}_4/\dot{\theta}_1$ (between angular velocity of axle 4 and angular velocity of blade 1); $\tau_{y41} = \dot{y}_4/\dot{\theta}_1$ (between lateral linear velocity of axle 4 and angular velocity of blade 1). Near configuration $\theta_1 = 0$ (undeformed fork), the values of velocity ratios are: $\tau_{21} = 0.99. \tau_{41} = 0.19$, $\tau_{y41} = 0.28\, m$. Since only small rotations are considered (they represent fork deformation), these ratios may be assumed to be constant. Value $\tau_{21} \approx 1$ means that the two blades in fact have the same rotation, whereas value $\tau_{41} = 0.19$ means that axle rotation is a small fraction of blade rotation.

These velocity ratios can be used to transform the four-bar linkage into an equivalent bar rotating about a revolute joint (rotation $\beta_f = \theta_1$) equipped with a rotational spring $k_{\beta f}$, (Fig. 6).

The moment of inertia of the equivalent bar is given by equation 1:

$$I^* = I_1 + I_2\tau_{21}^2 + I_{G4}\tau_{41}^2 + m_4\tau_{y41}^2 \quad (1)$$

where $I_1 = I_2 = 0.0079\ \text{kg}\cdot\text{m}^2$ are the moments of inertia of blades 1 and 2 about points O_1 and O_2, $I_{G4} = 0.00016\ \text{kg}\cdot\text{m}^2$ is the moment of inertia of axle 4 about its centre of mass, and $m_4 = 0.079\ \text{kg}$ is the mass of the axle (the wheel is not taken into account). The resulting moment of inertia of the equivalent bar is $I^* = 0.0219\ \text{kg}\cdot\text{m}^2$. The stiffness of the equivalent spring is:

$$k_{\beta f} = k_\theta + k_\theta \tau_{21}^2 = 2k_\theta \tag{2}$$

The natural frequency of the equivalent bar is:

$$f_n = \frac{1}{2\pi}\sqrt{\frac{k_{\beta f}}{I^*}} \tag{3}$$

Since the equivalent moment of inertia is obtained from the mass properties of the fork and the natural frequency can be set at the natural frequency of the lateral mode of the fork, equivalent stiffness $k_{\beta f}$ can be calculated from equation (3): $k_{\beta f} = 4725\ \text{N}\cdot\text{m/rad}$.

A static test was also performed, in order to verify this value of fork stiffness. Increasing loads were applied to the axle in lateral direction y, and displacements were measured on a dial gauge. The slope of the measured curve (Fig. 7) gives static stiffness in the lateral direction: $k_y = 55590\ \text{N/m}$.

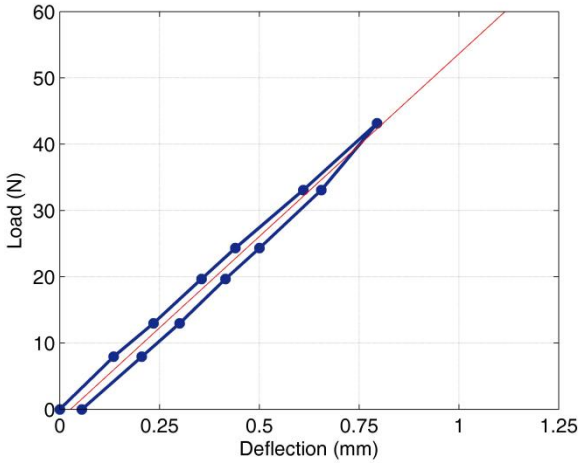

Figure 7. Static stiffness curve of fork in lateral direction.

The equivalent rotational stiffness can be calculated according to the model of Figure 6. Since velocity ratio τ_{21} is about 1, blades 1 and 2 move together and the two rotational stiffnesses are in parallel ($k_{\beta f} = 2k_\theta$). Equation 4 between linear stiffness at the axle and angular stiffness holds true:

$$k_y = 2k_\theta \left(\frac{\dot{\theta}_1}{\dot{y}_4}\right)^2 = k_{\beta f}\frac{1}{(\tau_{y41})^2} \tag{4}$$

Therefore, the rotational stiffness equivalent to the measured linear stiffness is:

$$k_{\beta f} = k_y \tau_{y41}^2 = 4349\ \text{N}\cdot\text{m/rad} \tag{5}$$

This value is only slightly lower than that identified from dynamic tests.

2.6 Identification of wheel stiffness

This section describes the lumped stiffness of the wheel, representing its behaviour when the diametric mode is excited. The rim with the tyre vibrates like a rigid ring, owing to spoke deformation; the wheel can therefore be modelled as a 1-DOF system in which the spokes behave like a mass-less spring of stiffness $k_{\beta w}$ about the diameter, and the whole inertia of the wheel is concentrated on the rigid ring (due to the small contribution of the spokes to wheel inertia).

The natural frequency of this system is given by:

$$f_n = \frac{1}{2\pi}\sqrt{\frac{k_{\beta w}}{I_{xx}}} \tag{6}$$

A trifilar pendulum was used to measure the moment of inertia of the wheel about its diameter (I_{xx}) resulting in $I_{xx} = 0.095\ \mathrm{kg \cdot m^2}$. Lastly, wheel stiffness was identified from equation (6):

$$k_{\beta w} = (2\pi f_n)^2\, I_{xx} = 2888\ \mathrm{N \cdot m/rad} \tag{7}$$

This value is markedly smaller than that of front fork stiffness $(4725\ \mathrm{N \cdot m/rad})$, and confirms that the wheel is a critical component from the viewpoint of front assembly compliance.

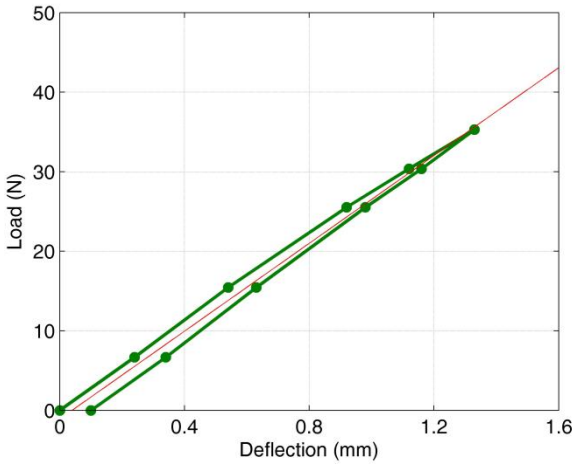

Figure 8. Static stiffness of wheel about diameter.

Also in this case, the stiffness value identified by modal analysis was compared with that obtained from a static test: one point on the wheel rim was loaded with increasing forces perpendicular to the wheel plane and displacements were measured on a dial gauge. The slope of the measured curve gave linear stiffness k_y (Fig. 8). The equivalent rotational stiffness about the wheel diameter is:

$$k_{\beta w} = k_y r_F^2 \tag{8}$$

in which r_F is wheel radius. The identified value, $2940\ \mathrm{N \cdot m/rad}$, matches that from modal analysis.

2.7 Lumped element model of front assembly compliance

The results of modal testing of the front assembly (Fig. 5), show that wheel rotation mainly depends on excitation of the diametric mode, due to spoke deformation, whereas the lateral displacement of the point of contact of the wheel depends on both the lateral mode of the fork and the diametric mode of the wheel. The front assembly model shown in Figure 9 was developed to represent this behaviour. It derives from the fork model of Figure 6, with the addition of the wheel, which was connected to the axle by a revolute joint and a rotational spring (stiffness $k_{\beta w}$), representing the stiffness of the spokes. This model has 2 DOF. Due to the geometry of the four-bar linkage, which is nearly a parallelogram, wheel rotation mainly depends on spoke deformation, whereas the lateral translation of the point of contact of the wheel depends on both spoke deformation (rotation β_w) and fork blade deformation (rotation β_f).

As it is rather difficult to add a 2-DOF model to the WCBM, an equivalent 1-DOF model was developed, which can generate the same behaviour of the front assembly when lateral force F_{Fy} is applied to the point of contact of the wheel with the road surface. In this model (Fig. 9), the fork is represented by a simple bar, divided into two parts by a revolute joint. A lumped spring (stiffness k_β) opposes the relative rotation β between the parts of the bar. The wheel is rigidly clamped to the tip of the bar. The distance between the wheel hub and the revolute joint is represented by h_W.

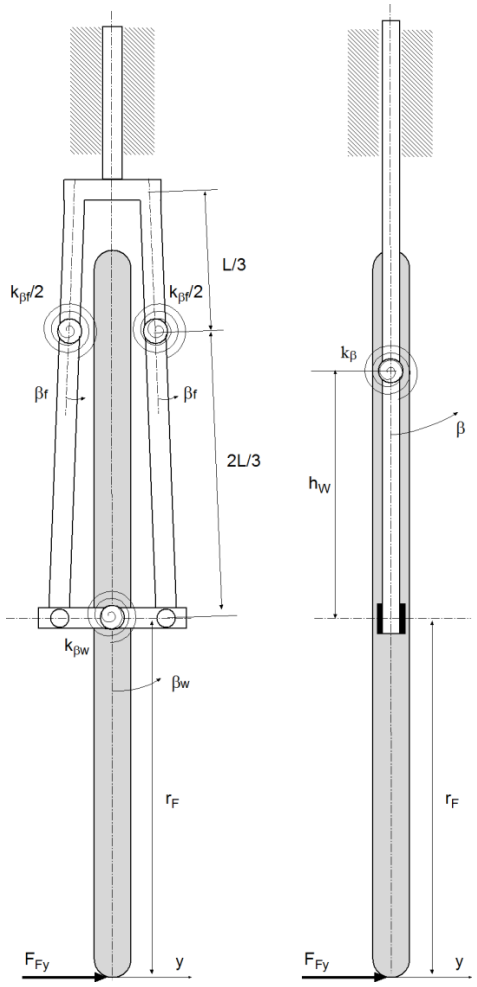

Figure 9. Lumped element model of front assembly.

Stiffness k_β and distance h_W of the equivalent system were calculated, taking into account the fact that lateral force F_{Fy} must generate the same rotation of the wheel and the same lateral displacement. The condition on wheel rotation is:

$$\beta_W = \beta \tag{9}$$

On the left, only the contribution of wheel deformation is considered, since that of the four-bar linkage to wheel rotation is very small. Taking into account the relations between rotations and moments caused by lateral force F_{Fy}, equation (9) becomes:

$$\frac{F_{Fy} r_F}{k_{\beta W}} = \frac{F_{Fy}(r_F + h_W)}{k_\beta} \tag{10}$$

The condition on lateral displacement *y* is:

$$\frac{2}{3}\beta_f L + \beta_W r_F = \beta(r_F + h_W) \tag{11}$$

On the left, the first contribution comes from the linkage and the second from the wheel. When the condition of equation (9) is introduced, equation (11) becomes:

$$\beta_f \frac{2}{3} L = \beta_w h_W \tag{12}$$

Taking into account the geometry of the linkage and the relations between rotations and moment caused by F_{Fy}, equation (12) becomes:

$$\frac{F_{Fy}\left(\frac{2}{3}L\right)^2}{k_{\beta f}} = \frac{F_{Fy} r_F h_W}{k_{\beta w}} \tag{13}$$

Hence, distance h_W can be calculated:

$$h_W = \frac{k_{\beta w}}{k_{\beta f}} \frac{\left(\frac{2}{3}L\right)^2}{r_F} \tag{14}$$

Stiffness k_β can be calculated by introducing equation (14) into equation (10):

$$k_\beta = k_{\beta w} + \frac{{k_{\beta w}}^2}{k_{\beta f}} \frac{\left(\frac{2}{3}L\right)^2}{r_F^2} \tag{15}$$

The calculated parameters of the equivalent 1-DOF system were thus: $h_W = 0.137$ m and $k_\beta = 4018\,\mathrm{N \cdot m/rad}$. This stiffness value clearly matches the results reported by Klinger (2014) and Limebeer (2006).

3 Bicycle model with front frame compliance

The bicycle model was extended to take into account bending compliance of the front assembly (see Fig. 10). Forward speed v is assumed to be constant and the rider's hands do not control the handlebars.

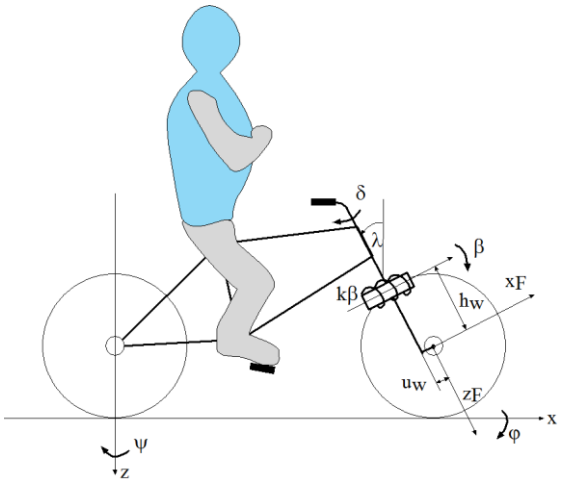

Figure 10. Bicycle model with bending compliance of front assembly.

The model is characterised by the presence of a revolute joint perpendicular to the steer axis which defines the deformation axis and divides the front assembly into two parts. A rotational spring with stiffness k_β and a rotational damper with constant c_β (not shown in Fig. 10) oppose rotation β and angular velocity $\dot{\beta}$ respectively.

It should be noted that, in Figure 10, constants k_β and c_β represent the stiffness and damping properties of the front assembly, because the position of deformation axis h_W lies along the fork span. But the same model can also represent compliance by the front wheel or steer head. In the former case, the deformation axis crosses the centre of the wheel ($h_W = 0$) and stiffness and damping parameters represent its compliance about a diametrical axis. In the latter case, the deformation axis crosses the steer head and the stiffness and damping parameters represent the torsional compliance of the chassis, which causes lateral displacement of the front wheel.
The equations of linearised WCBM derive from angular momentum balances (Meijaard, 2007). The first equation (roll) derives from the roll angular momentum balance for the whole bicycle (including its rider) about a fixed axis in the road plane, which is instantaneously aligned with the line where the rear frame of the bicycle intersects the road plane. The second equation (yaw) derives from the yaw angular momentum balance for the whole bicycle about a fixed vertical axis which instantaneously passes through the contact point of the rear wheel. The third equation (steer) derives from steer angular momentum balance of the front frame about the steer axis.
In the model, rotation β of the front wheel about the deformation axis generates new linear and angular momentum components which must be taken into account in the equations.
The new linear momentum is given by equation (16), in which m_F is the front wheel mass, h_W the distance between the bending axis and the centre of mass of the wheel, and $\hat{\jmath}$ is the unit vector perpendicular to the bicycle plane:

$$P_W = -m_F h_W \dot{\beta} \hat{\jmath} \tag{16}$$

The corresponding angular momentum components about the roll, steer and yaw axes are shown in equation (17), where r_F, u_W and w are front wheel radius, wheel offset, and wheelbase, respectively:

$$\begin{Bmatrix} Mm_\varphi \\ Mm_\delta \\ Mm_\psi \end{Bmatrix} = \begin{Bmatrix} -m_F h_W r_F \dot{\beta} \\ -m_F h_W u_W \dot{\beta} \\ -m_F h_W w \dot{\beta} \end{Bmatrix} \tag{17}$$

Euler's equation applied to the front wheel in the front wheel frame of reference (x_F, y_F, z_F) is then developed to calculate the new angular momentum components due to $\dot{\beta}$ and the inertia tensor of the wheel:

$$
\begin{aligned}
&{}^{F}\begin{bmatrix} I_{Fxx} & 0 & 0 \\ 0 & I_{Fyy} & 0 \\ 0 & 0 & I_{Fzz} \end{bmatrix} {}^{F}\begin{Bmatrix} \alpha_x \\ \alpha_y \\ \alpha_z \end{Bmatrix} + {}^{F}\begin{bmatrix} 0 & -\omega_z & \omega_y \\ \omega_z & 0 & -\omega_x \\ -\omega_y & \omega_x & 0 \end{bmatrix} \times \\
&{}^{F}\begin{bmatrix} I_{Fxx} & 0 & 0 \\ 0 & I_{Fyy} & 0 \\ 0 & 0 & I_{Fzz} \end{bmatrix} {}^{F}\begin{Bmatrix} \omega_x \\ \omega_y - v/r_F \\ \omega_z \end{Bmatrix} = {}^{F}\begin{Bmatrix} M_x \\ M_y \\ M_z \end{Bmatrix}
\end{aligned}
\tag{18}
$$

In equation (18) $I_{Fxx} = I_{Fzz}$ is the moment of inertia of the front wheel about the diametric axis, I_{Fyy} the spin moment of inertia, and $-v/r_F$ the spin velocity of the front wheel. $\omega_x, \omega_y, \omega_z$ are the components of angular velocity of the front wheel due to roll ($\dot{\varphi}$), yaw ($\dot{\psi}$), steer ($\dot{\delta}$) and deformation velocity ($\dot{\beta}$); if second-order terms are neglected, they are given by:

$$
\begin{Bmatrix} \omega_x \\ \omega_y \\ \omega_z \end{Bmatrix} = \begin{Bmatrix} \dot{\varphi}\cos(\lambda) - \dot{\psi}\sin(\lambda) + \dot{\beta} \\ 0 \\ \dot{\varphi}\sin(\lambda) + \dot{\psi}\cos(\lambda) + \dot{\delta} \end{Bmatrix}
\tag{19}
$$

$\alpha_x, \alpha_y, \alpha_z$ are the components of angular acceleration of the front wheel:

$$
\begin{Bmatrix} \alpha_x \\ \alpha_y \\ \alpha_z \end{Bmatrix} = \begin{Bmatrix} \ddot{\varphi}\cos(\lambda) - \ddot{\psi}\sin(\lambda) + \ddot{\beta} \\ 0 \\ \ddot{\varphi}\sin(\lambda) + \ddot{\psi}\cos(\lambda) + \ddot{\delta} \end{Bmatrix}
\tag{20}
$$

After introducing equations (19) and (20), Euler's equation becomes:

$$
{}^{F}\begin{Bmatrix} MI_x \\ MI_y \\ MI_z \end{Bmatrix} \equiv {}^{F}\begin{Bmatrix} I_{Fxx}\left(\ddot{\varphi}\cos(\lambda) - \ddot{\psi}\sin(\lambda) + \ddot{\beta}\right) - \dfrac{I_{Fyy} v\left(-\dot{\varphi}\sin(\lambda) - \dot{\psi}\cos(\lambda) - \dot{\delta}\right)}{r_F} \\ 0 \\ I_{Fxx}\left(\ddot{\varphi}\sin(\lambda) + \ddot{\psi}\cos(\lambda) + \ddot{\delta}\right) - \dfrac{I_{Fyy} v\left(\dot{\varphi}\cos(\lambda) - \dot{\psi}\sin(\lambda) + \dot{\beta}\right)}{r_F} \end{Bmatrix} = {}^{F}\begin{Bmatrix} M_x \\ M_y \\ M_z \end{Bmatrix}
\tag{21}
$$

M_x, M_y, M_z are the components of the moments of external forces about the centre of mass of the front wheel. In particular, M_x (about the x_F axis parallel to the deformation axis) is given by the following equation:

$$
{}^{F}M_x = h_W R_y - k_\beta \beta - c_\beta \dot{\beta} - r_F \cos(\lambda) F_{Fy} + g R_W \left(\varphi + \delta \sin(\lambda) + \beta \cos(\lambda)\right)
\tag{22}
$$

The first term is the moment of the lateral reaction force transmitted through the revolute joint:

$$
R_y = \ddot{y}_F m_F - F_{Fy}
\tag{23}
$$

In equation (23), F_{Fy} is the lateral ground force and $\ddot{y}_F$ is the linear acceleration of the front wheel centre of mass, which depends on the linear acceleration of the rear contact point P ($\ddot{y}_P$) and on angular accelerations:

$$\ddot{y}_F = \ddot{y}_P + w\ddot{\psi} + r_F\ddot{\varphi} + u_W\ddot{\delta} - h_W\ddot{\beta} \tag{24}$$

The terms of equation (22) depending on β and $\dot{\beta}$ are the effects of elastic and damping forces. The fourth term depends on lateral ground force. The last term takes into account the moment caused by the front vertical ground reaction and vertical reaction force transmitted through the revolute joint. Constant R_W is given by equation (25):

$$R_W = \left(\frac{m_T x_T}{w} \left(h_W + r_F \cos(\lambda) - m_F h_W \right) \right) \tag{25}$$

In equation (25), m_T is total mass and x_T the horizontal position of the global centre of mass. The first of equations (21) (about axis x_F parallel to the deformation axis) is added to the other angular momentum equations and is the fourth equation of the model.
The new terms deriving from deformation of the front frame are added to the equations for roll, steer and yaw, calculated projecting the left-hand side of equation (21) on the roll (x), yaw (z) and steer axes and selecting the new terms depending on $\dot{\beta}$ and $\ddot{\beta}$. The projection equations are:

$$\begin{Bmatrix} MI_x \\ MI_y \\ MI_z \end{Bmatrix} = \begin{bmatrix} 1 & 0 & 0 \\ 0 & 1 & -\varphi \\ 0 & \varphi & 1 \end{bmatrix} \begin{bmatrix} \cos(\lambda) & 0 & \sin(\lambda) \\ 0 & 1 & 0 \\ -\sin(\lambda) & 0 & \cos(\lambda) \end{bmatrix} \begin{bmatrix} 1 & -\delta & 0 \\ \delta & 1 & 0 \\ 0 & 0 & 1 \end{bmatrix} \begin{bmatrix} 1 & 0 & 0 \\ 0 & 1 & -\beta \\ 0 & \beta & 1 \end{bmatrix}^F \begin{Bmatrix} MI_x \\ MI_y \\ MI_z \end{Bmatrix} \tag{26}$$

$$^{steer}\begin{Bmatrix} MI_x \\ MI_y \\ MI_z \end{Bmatrix} = \begin{bmatrix} 1 & 0 & 0 \\ 0 & 1 & -\beta \\ 0 & \beta & 1 \end{bmatrix}^F \begin{Bmatrix} MI_x \\ MI_y \\ MI_z \end{Bmatrix} \tag{27}$$

The superscript "*steer*" indicates the steer coordinate system with axis z aligned with the steer axis. The trigonometric functions of small angles are linearised in the rotation matrices.
The four equations of the model contain five unknowns. They are $\varphi, \delta, \psi, \beta$ and the lateral ground force at front contact point F_{Fy}. F_{Fy} appears in the yaw, steer and front wheel equation, and this unknown is eliminated by means of the yaw equation, like Meijaard does (2007). Lastly, yaw velocity and acceleration are eliminated by means of rolling-contact lateral constraints:

$$\dot{\psi} = \frac{v(\delta\cos(\lambda) - \beta\sin(\lambda)) + c\dot{\delta}\cos(\lambda)}{w} + \frac{h_W + r_F\cos(\lambda)}{w}\dot{\beta} \tag{28}$$

$$\ddot{\psi} = \frac{v(\dot{\delta}\cos(\lambda) - \dot{\beta}\sin(\lambda)) + c\ddot{\delta}\cos(\lambda)}{w} + \frac{h_W + r_F\cos(\lambda)}{w}\ddot{\beta} \tag{29}$$

$$\ddot{y}_P = v\dot{\psi} \tag{30}$$

Symbol c represents the trail of the bicycle (Meijaard, 2007). It should be noted that, if the front assembly is rigid ($\beta = \dot{\beta} = \ddot{\beta} = 0$), the last three equations become those presented by Meijaard (2007).
The final set of equations includes three linear second-order coupled equations in variables φ, δ, β. They represent free oscillations of the system and are useful for studying uncontrolled stability

(when the rider does not hold the handlebars). The structure of these equations is similar to that of the WCBM:

$$[M]\begin{Bmatrix}\ddot{\varphi}\\ \ddot{\delta}\\ \ddot{\beta}\end{Bmatrix} + v[C_1]\begin{Bmatrix}\dot{\varphi}\\ \dot{\delta}\\ \dot{\beta}\end{Bmatrix} + \left[g[K_0] + v^2[K_2]\right]\begin{Bmatrix}\varphi\\ \delta\\ \beta\end{Bmatrix} + [C]\begin{Bmatrix}\dot{\varphi}\\ \dot{\delta}\\ \dot{\beta}\end{Bmatrix} + [K]\begin{Bmatrix}\varphi\\ \delta\\ \beta\end{Bmatrix} = \begin{Bmatrix}0\\ 0\\ 0\end{Bmatrix} \tag{31}$$

Matrices $[M]$, $[C_1]$, $g[K_0]$, $v^2[K_2]$ have the same meaning as the corresponding WCBM matrices, but have dimension 3x3 and account for the additional terms due to front assembly deformation, when they occur. Matrices $[C], [K]$ are the "true" damping and stiffness matrices and take into account the stiffness and damping properties of the front assembly. Matrix coefficients are listed in Appendix 1. The bicycle model with fork compliance was implemented in a MATLAB code. The complex eigenvalue problem was solved in order to perform stability analysis.

4 Parametric analysis

In order to rank the influence of bicycle parameters on stability, a series of numerical simulations was planned. The bicycle parameters included geometric and mass properties and front assembly stiffness. As regards the former, a rigid bicycle is described by 25 parameters (Meijaard, 2007). A reduced set of these parameters was taken into account here for the following reasons: some preliminary analyses had shown that some parameters had a negligible effect on stability; some were functions of other parameters (e.g., the mass and inertia properties of a wheel are functions of wheel radius). Rear mass and inertia actually depend on the rider, whose mass cannot be considered as a design parameter.

Figure 11 shows the eight geometric and mass parameters chosen: front and rear wheel radii (r_F and r_R), handlebar and fork assembly mass (m_H), longitudinal and vertical position of the centre of mass (x_B and z_B), wheelbase (w), caster angle (λ) and trail (c). Note that, in parametric analysis, when r_F and r_R were varied, the mass and moment of inertia of the wheels also varied. Fitting curves derived from the measured values were used to calculate the proportions between wheel radius and mass properties.

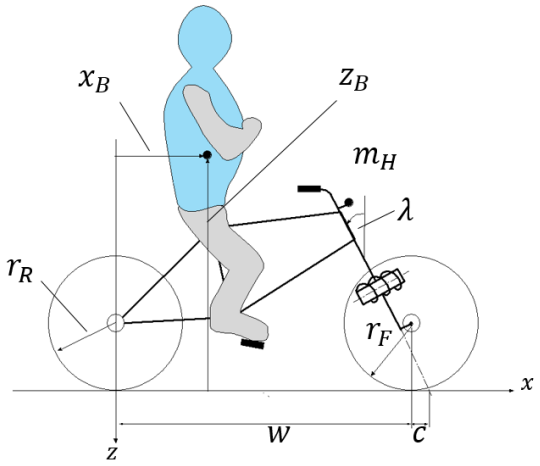

Figure 11. Bicycle parameters.

Our aim was to analyse the influence on the stability of the selected parameters one at a time. This approach poses some problems when variations in w, c and λ are involved, because the coordinates of m_H are defined with respect to coordinate system xyz (with its origin at the rear contact point) and any variations in w, c and λ, which define the position of the steer axis, can modify the position of m_H with respect to the steer axis, thus introducing an additional dynamic effect. To give an example, Figure 12 shows the effect of a variation in trail c. In this case, u_H, which is defined as the distance between the centre of mass of the front assembly and the steer axis, changes. To avoid this effect, a kinematic analysis was carried out to correct the position of m_H with respect to xyz and to maintain the distance of m_H from the steer axis constant.

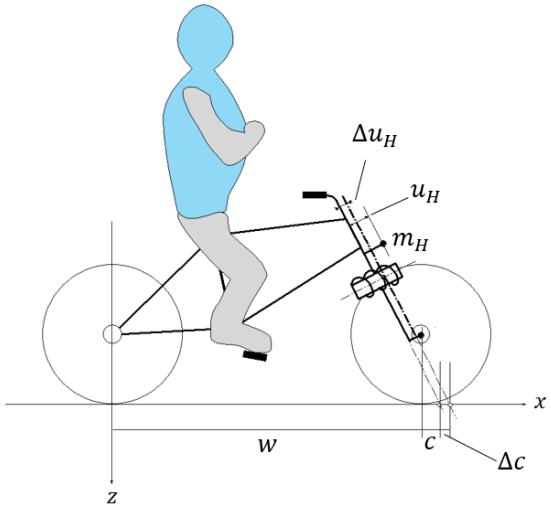

Figure 12. Effect of c on distance between m_H and steer axis.

As regards stiffness parameters, the equivalent rotational stiffness about the wheel diameter (equation 8) and the equivalent front assembly stiffness (equation 15) were taken into account in parametric analysis. The corresponding damping coefficients are difficult to estimate. Damping coefficients identified from modal tests on single components may underestimate those of the low-frequency modes of the whole bicycle, which are largely affected by connections between elements. The stiffness parameters identified here match those reported by Limebeer (2006), Sharp (2008) and Klinger (2014). These authors also report damping coefficient values. For the above-mentioned reasons, damping coefficient c_β about the deformation axis was set at 20 N·m·s/rad for stiffness $k_\beta = 2000$ N·m/rad, which are the values reported in Limebeer (2006). When different stiffness values were adopted, the damping coefficient was modified according to equation (32) in order to keep the damping ratio constant.

$$c_\beta = 20\sqrt{\frac{k_\beta}{2000}} \tag{32}$$

For each design parameter, one low level and one high level were defined (see Table 4). The numerical values of the two levels were selected according to the following criteria:

1) Their average values must be equal to the corresponding design parameter of the benchmark bicycle presented by Meijaard (2007).

2) High and low levels of the parameter must be compatible with a real-life bicycle.
3) The ranges of the various parameters must be similar.

In order to reduce the number of simulations and for more information on the effects of bicycle characteristics on stability, the first parametric analysis was carried out considering a rigid bicycle, so that only the eight geometric and mass parameters were used. Analysis of the results revealed the least influential parameter. The following analyses were carried out by removing it from the list and introducing a compliance parameter in its place: wheel compliance or front assembly compliance. With this approach, each parametric analysis included $2^8 = 256$ simulations, because a full factorial experiment was planned (Montgomery, 2008).

Table 4. Design parameters.

Parameter	Nominal value	Low level	High level	Standard deviation / Nominal value
Rear wheel radius r_R	0.305 m (12 in)	0.254 m (10 in)	0.356 m (14 in)	0.167
Front wheel radius r_F	0.337 m (13.25 in)	0.305 m (12 in)	0.368 m (14.5 in)	0.0943
Handlebar and fork mass m_H	4 kg	3 kg	5 kg	0.25
Rear body and frame horizontal coordinate X_B	0.3 m	0.2 m	0.4 m	0.333
Rear body and frame vertical coordinate Z_B	-0.9 m	-0.75 m	-1.05 m	0.167
Wheelbase w	1.02 m	0.80 m	1.24 m	0.216
Trail c	0.08 m	0.05 m	0.11 m	0.375
Caster angle λ	18° [π/10 rad]	15° [π/12 rad]	21° [7 π/60 rad]	0.167
Wheel stiffness $k_{\beta w}$	2888 N · m/rad	2166 N · m/rad	3610 N · m/rad	0.25
Assembly stiffness k_β	4018 N · m/rad	3013 N · m/rad	5022 N · m/rad	0.25

5 Numerical Results

5.1 Eigenvalue plots

Numerical stability analysis was carried out with a MATLAB code which calculates the eigenvalues and eigenvectors for assigned values of forward speed. The typical output of the code is shown in Figure 13, which deals with the benchmark bicycle. The blue dots are the real parts and the purple circles are the imaginary parts of the eigenvalues.

For each eigenvalue plot, weave speed v_w and capsize speed v_c were identified. Weave speed is defined as the speed at which the weave mode becomes stable; capsize speed is the speed at which the capsize mode becomes unstable. The difference between these speeds determines the self-stability range.

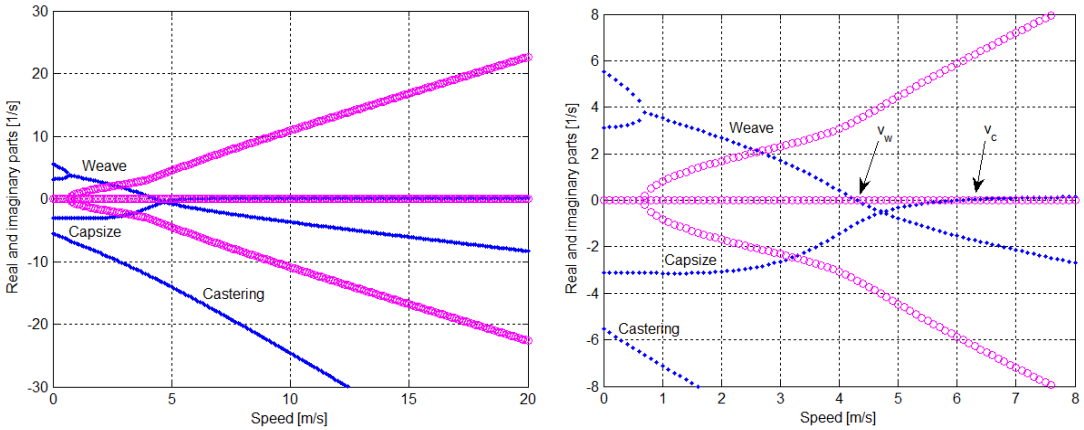

Figure 13. Eigenvalues of benchmark bicycle with rigid front assembly.

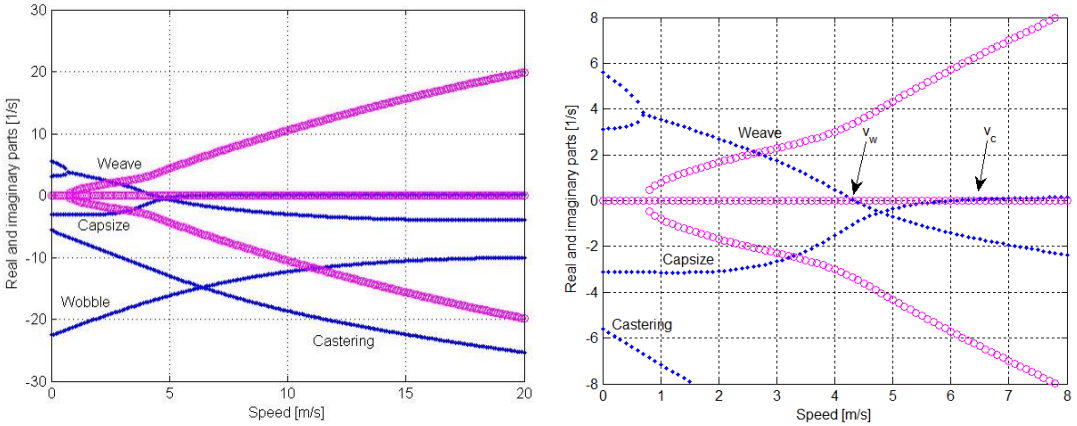

Figure 14. Eigenvalues of the benchmark bicycle with compliant wheel.

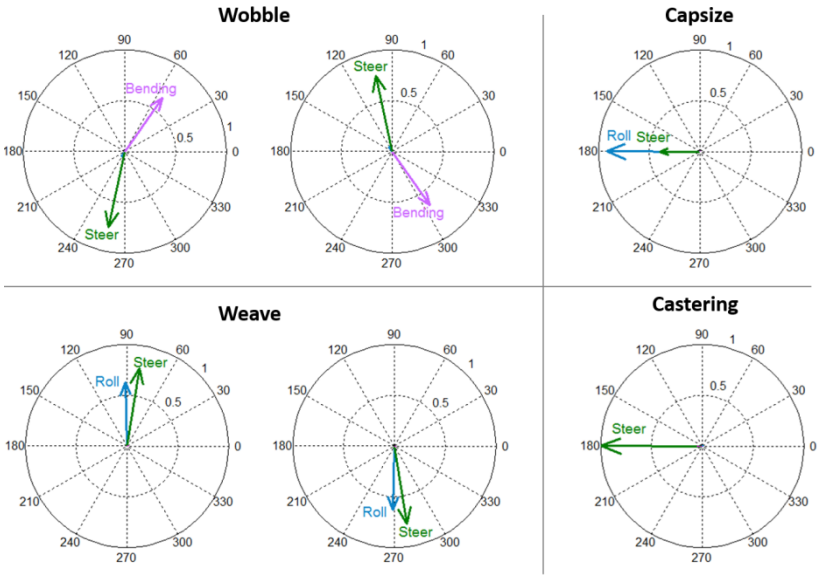

Figure 15. Modes of vibration of benchmark bicycle with compliant wheel at 5 m/s. Shapes are shown by vector diagrams. Arrows: amplitude and phase of modal components.

The eigenvalue plot of Figure 14 shows the effect of front wheel compliance on bicycle stability. The benchmark bicycle with $k_{\beta w} = 2888\ \mathrm{N \cdot m/rad}$, $c_{\beta w} = 24\ \mathrm{N \cdot m \cdot s/rad}$ (according to equation 32) and $h_w = 0\ \mathrm{m}$ is examined.

Capsize, weave and castering modes are only slightly affected by front wheel compliance. The real and imaginary parts of weave show small variations at high speed (20 m/s). Weave speed v_w and capsize speed v_c are not markedly affected by introducing the compliant wheel.

The main difference between Figures 13 and 14 is the appearance of a new complex mode. The vector diagrams of the modes (Fig. 15) show that the new mode is dominated by steer rotation and wheel bending. It is therefore a wobble mode caused by compliance, which changes the orientation of the front wheel and the position of the front contact point. Wobble (or shimmy) modes caused by compliance have been discussed by some authors who have examined bicycle stability (Klinger 2014) (Limebeer 2006) and motorcycle stability (Paceijka 2002).

The imaginary part of the eigenvalue of wobble does not appear in Figure 14, because the natural frequency is high (about 12 Hz at low speed). The real part of the eigenvalue is large and negative at zero speed; it then decreases in modulus. In the range of speeds considered here, which are compatible with bicycles, wobble is always stable, but at higher speeds it may become unstable. This trend is similar to that discussed by Limebeer (2006).

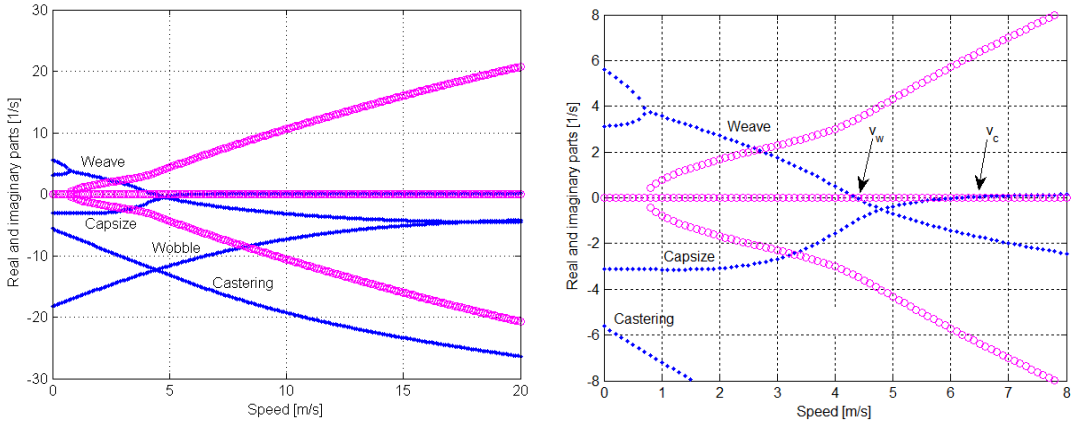

Figure 16. Eigenvalues of benchmark bicycle with compliant front assembly.

The effects of introducing front assembly compliance on the eigenvalue plot is shown in Figure 16. The benchmark bicycle with $k_\beta = 4018\ \mathrm{N \cdot m/rad}$, $c_\beta = 28.3\ \mathrm{N \cdot m \cdot s/rad}$ (according to equation 32) and $h_w = 0.137\ \mathrm{m}$ is examined. Also in this case, capsize, weave and castering modes are not greatly affected. The wobble mode still takes place at high frequency, but the curve of the real part of the eigenvalue shows that this mode is less damped than Figure 14 shows.

5.2 Correlation analysis

Three parametric analyses were performed: 1) the bicycle was considered rigid; 2) wheel compliance was included; 3) front assembly compliance was included. In each parametric analysis, the eigenvalue plots obtained with 256 combinations of parameters were taken into account, to show the effects of the various parameters on bicycle stability (see Figure 17). Weave speed v_w and capsize speed v_c were identified for each eigenvalue plot. The difference between these speeds determined the self-stability range. Then a self-stability area was calculated in the eigenvalue plot as the area defined by the speed axis and the real parts of the weave and capsize eigenvalues when both were negative (see Figure 18). In order to calculate the self-stability area, the weave and capsize curves were fitted with two polynomial functions and the integral of the functions between v_w and v_c was calculated. The self-stability area in fact depends not only on the self-stability range, but also on the distance between stable eigenvalues and the condition of instability.

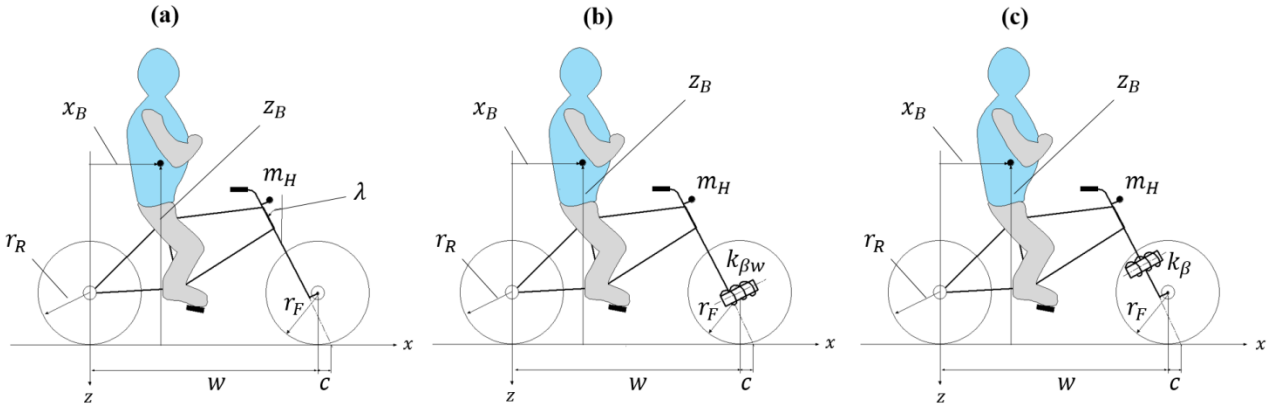

Figure 17. (a) Rigid bicycle. (b) Bicycle with wheel compliance. (c) Bicycle with front assembly compliance.

Since numerical values are needed to evaluate the effect of the design parameters on weave speed, capsize speed, self-stability range and self-stability area, the numerical results were re-processed to calculate Bravais Pearson correlation coefficients ρ_{xy} (Box, 2005):

$$\sigma_x^2 = \frac{1}{n}\sum_{i=1}^{n}(x_i - \bar{x})^2 \tag{33}$$

$$\sigma_y^2 = \frac{1}{n}\sum_{i=1}^{n}(y_i - \bar{y})^2 \tag{34}$$

$$\sigma_{xy} = \frac{1}{n}\sum_{i=1}^{n}(x_i - \bar{x})(y_i - \bar{y}) \tag{35}$$

$$\rho_{xy} = \frac{\sigma_{xy}}{\sigma_x \sigma_y} \tag{36}$$

In the present case, σ_y is the square root of the variance of an output (e.g., capsize speed), y_i are the values measured in the 256 tests, and $\bar{y}$ is the arithmetic average of y_i. σ_x is the square root of the variance of a design parameter (e.g., wheelbase), x_i are the levels, and $\bar{x}$ is the arithmetic average of x_i. σ_{xy} is the covariance between an output and a design parameter. The correlation coefficient represents the normalised measure of the strength of relationship between variables, and ranges from −1 to 1. Values close to 1 indicate a strong linear positive relationship between the variables; values close to −1 indicate a strong linear negative relationship between them (anti-correlation); values close or equal to 0 indicate no evidence of any relationship between variables.

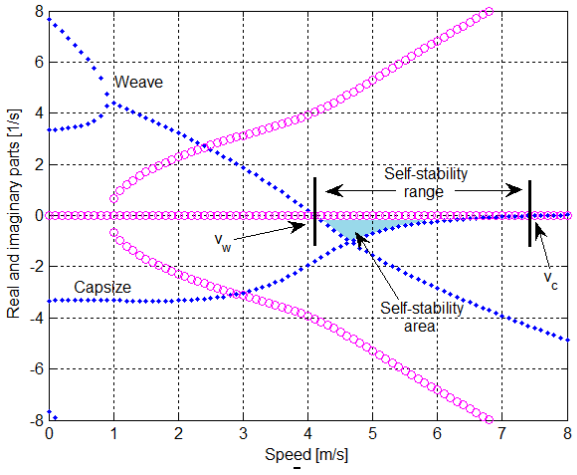

Figure 18. Definition of stability indexes.

Figure 19 shows the correlation coefficients and the eight design parameters of the rigid bicycle model. A closer look at the correlation coefficients between weave speed and design parameters shows that the former decreases greatly (stabilising effect) if the front radius is increased, increases

greatly when trail increases (destabilising effect) and increases moderately when wheelbase and caster angle increase. These data match the trends of weave speed reported by Moore (2006). As here the increment in r_F leads to an increment in the spin moment of inertia of the wheel, this result also matches those reported by Plochl (2012), who examined variations in the spin moment of inertia. The correlation coefficients of the other four parameters are very small and show that these parameters do not significantly affect weave speed.

As regards capsize mode, the correlation coefficients show that the effect of front wheel radius and trail on capsize stability is the opposite of that for weave stability: the front wheel radius has a strong destabilising effect, whereas the trail has a significant stabilising effect. These results match those of Moore (2006).

A large stabilising effect is caused by the forward displacement of the centre of mass of the bicycle along horizontal axis x_B. The other five parameters have little effect on capsize speed.

Taking into account the self-stability area and range, the rear wheel radius reveals a moderate stabilising effect. Instead, the front wheel radius has a significant destabilising effect: if this radius increases, bicycle stability decreases. The mass of the front assembly has a small stabilising effect.

The longitudinal position of the centre of mass of the rear frame has a considerable effect on self-stability range and area: when the centre of mass moves forward, stability increases, due to the large effect of x_B on capsize speed. If the height of the centre of mass decreases, parameter z_B increases (because axis z points downwards) and correlation analysis shows a small increase in self-stability area and range. These results match those of the effect of rider position on stability found by Williams (2015).

Wheelbase and trail have opposite effects on bicycle stability: when the wheelbase increases, stability decreases; when the trail increases, so does stability. Lastly, an increase in caster angle has a small negative effect on self-stability area and range.

The self-stability area and range indexes essentially give similar information. When there is some difference between them (e.g., in the case of caster angle λ), the indication given by the self-stability area must be viewed as more reliable, because the self-stability area captures more details of the eigenvalue plot.

The first cycle of 256 simulations showed that the caster angle has a minimum effect on bicycle stability. Front wheel stiffness was introduced and the caster angle was removed from the set of parameters for the second cycle.

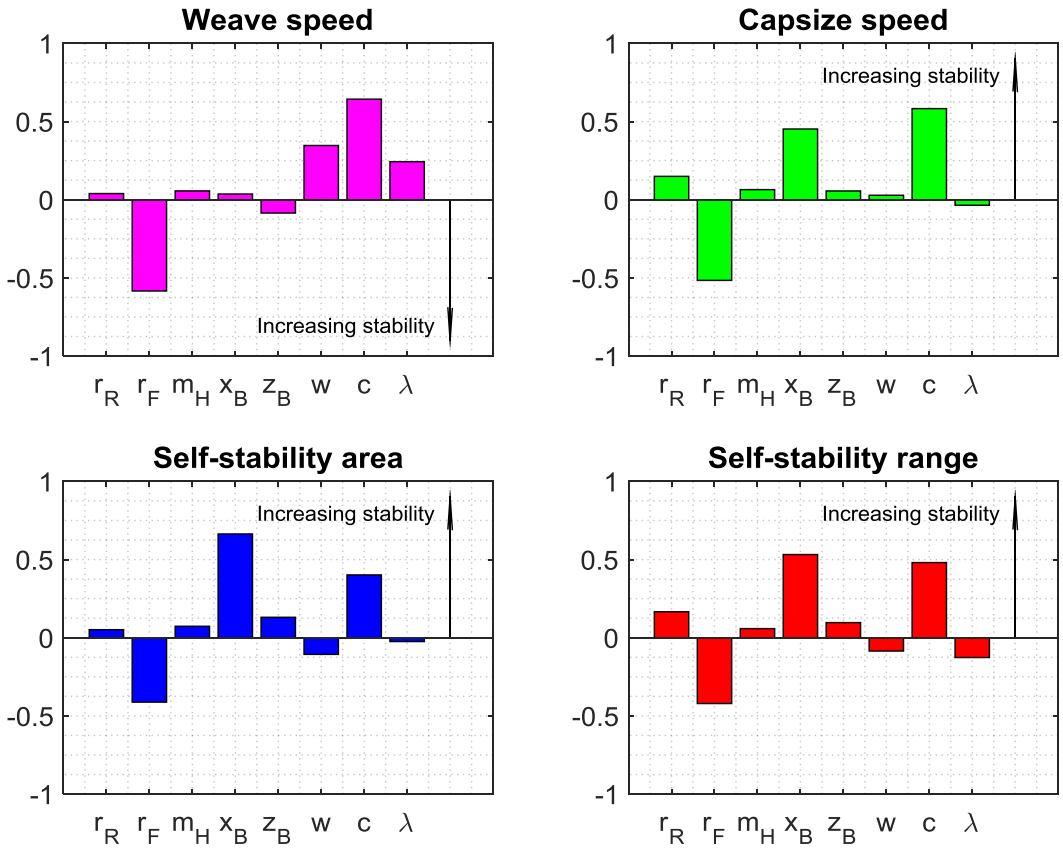

Figure 19. Results of correlation analysis results, rigid bicycle.

The results of these simulations are shown in Figure 20. The introduction of front wheel compliance does not significantly affect the overall aspect of the histograms. As regards weave speed, the moduli of the indexes for front wheel radius, longitudinal position of the centre of mass and wheelbase show small increases, the first with a stabilising effect and the others with a destabilising one. Capsize speed is less affected by the introduction of front wheel compliance, as only small increments in the indexes of the longitudinal position of the centre of mass and wheelbase are measured. As regards self-stability area and range, small increments were measured in the moduli of the coefficients of wheelbase and the longitudinal position of the centre of mass, and a small decrement in the module of the trail index. They indicate that the influence on the self-stability of the geometric and mass parameters remains similar when wheel compliance is included. In addition, Figure 20 shows that front wheel stiffness has a negligible effect on bicycle stability.

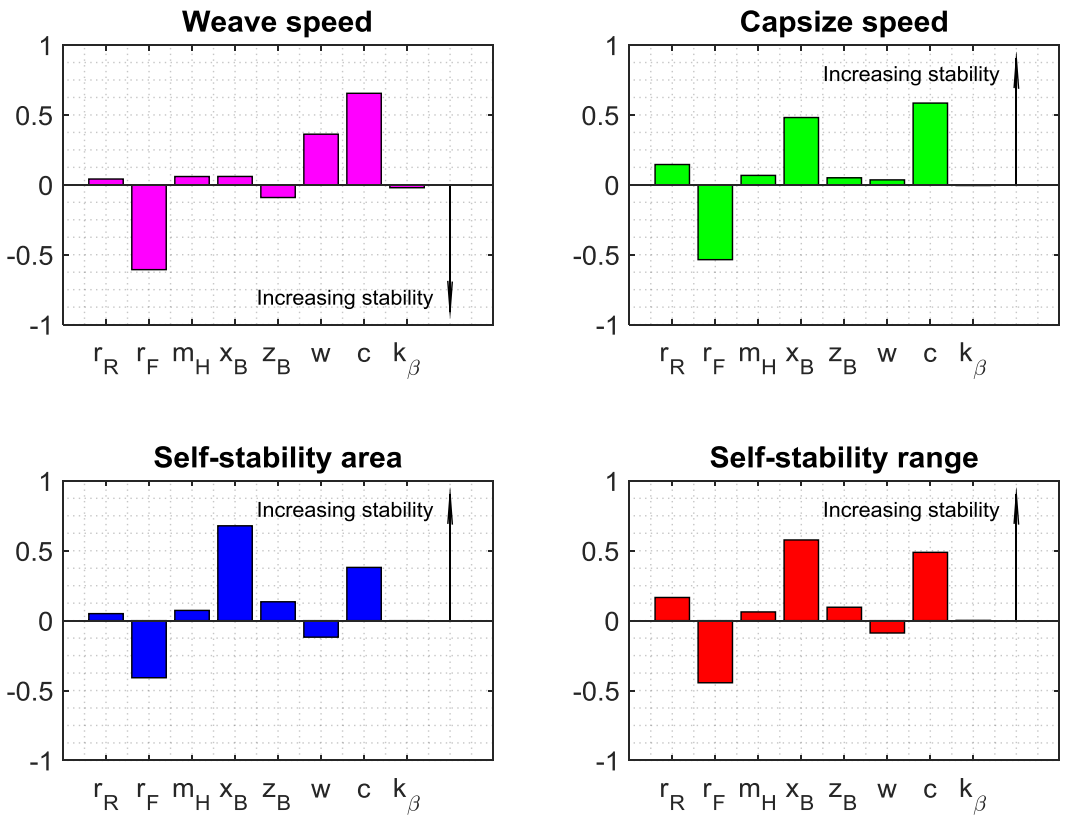

Figure 20. Correlation analysis results, bicycle with compliant wheel.

The third cycle of simulations was carried out on the combined effect of fork and wheel compliances, as shown in Figure 21: the variations are very small with respect to Figure 20. The bending compliance of the front assembly has a small destabilising effect.

In the previous analyses, the damping coefficient was held constant. Figure 22 shows the effect of variations in damping coefficient with compliant front assembly ($k_\beta = 4018\,\mathrm{N\cdot m/rad}$ and $h_w = 0.137$ m). When the damping coefficient is halved ($c_\beta = 14.2$ N·m·s/rad), wobble becomes unstable at 7.5 m/s, which is above the self-stability range. When the damping coefficient is reduced by ten ($c_\beta = 2.83$ N·m·s/rad), wobble becomes unstable at low speed (about 1.3 m/s). In this case, the self-stability range has no meaning, since wobble is already unstable. It should be noted that, if damping coefficient c_β is halved, the self-stability range only varies from 1.756 to 1.755 m/s.

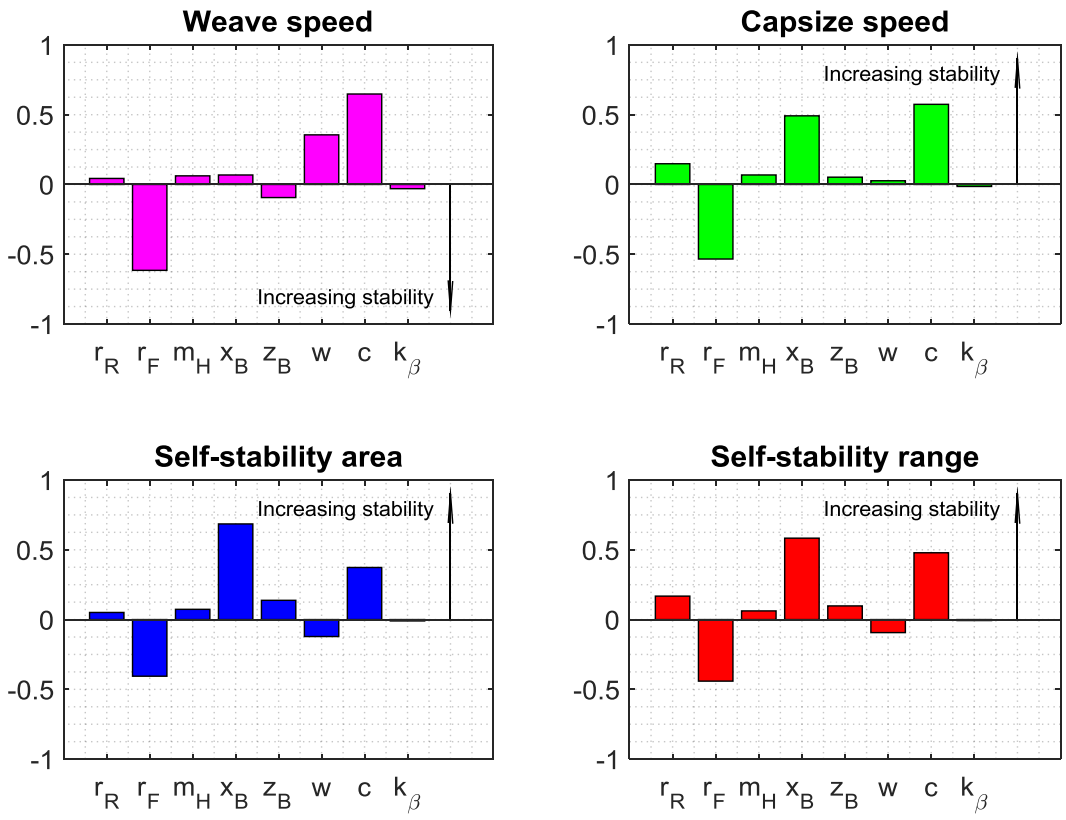

Figure 21. Correlation analysis results, bicycle with compliant front assembly.

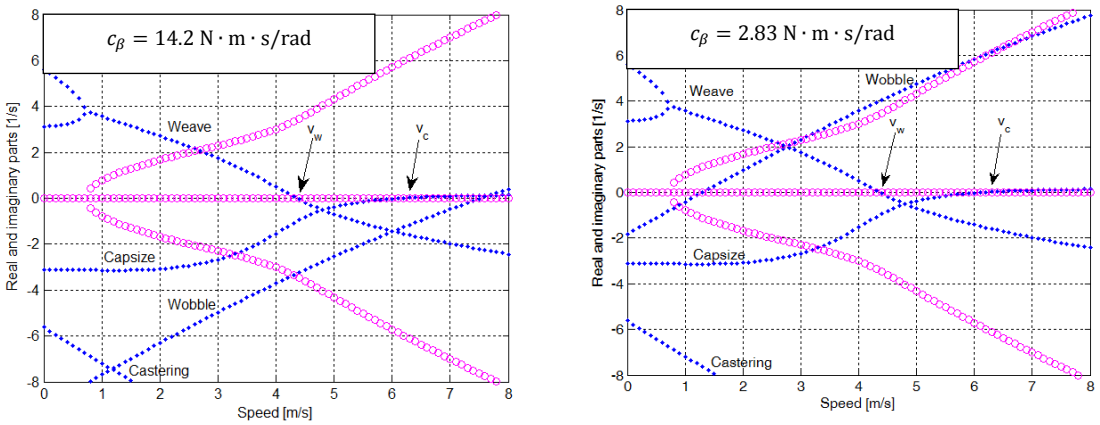

Figure 22. Eigenvalues of bicycle with compliant front assembly and decreasing values of damping.

Lastly, the effects of wheel and front assembly compliance on self-stability were compared with those caused by other extensions of the WCBM reported in the literature. The benchmark bicycle parameters were used for comparison.

Table 5 shows that introducing a linear tyre model has a greater effect than that of structural and rider compliance. A similar analysis was provided by Plöchl (2012), although a different bicycle was used; results show that tyre properties have the greatest effect on capsize and weave speed, followed by structural and rider compliance.

Table 5. Self-stability ranges for various model extensions.

Model	v_w [m/s]	v_c [m/s]	Stability range [m/s]	Reference
WCBM	4.292	6.024	1.732	Meijaard 2007
With wheel compliance	4.344	6.061	1.717	Figure 14
With front assembly compliance	4.358	6.114	1.756	Figure 15
With linear tyre model	4.1*	5.4*	1.3*	Sharp 2008
With rider torsion compliance	4.291	6.024	1.733	Doria 2014
With rider leaning sideways	4.237	6.018	1.781	Doria 2014

*Data obtained from plot in which only two digits are significant.

6 Conclusions

Experimental results obtained with the modal analysis approach show that wheel compliance has a considerable effect on the compliance of the front assembly of a standard bicycle. Deformation of fork blades contributes to lateral displacement of the wheel, but has little effect on its attitude. A method for calculating the equivalent stiffness of the front assembly from experimental results is presented and the WCBM is extended to include front assembly compliance.

Stability analysis results show that front assembly compliance generates a new mode, i.e., wobble, dominated by rotations about the deformation and steer axes. The wobble mode is stable in the range of speeds suitable for a bicycle, if the damping coefficient about the deformation axis is greater than 15-20 N·m·s/rad. Front assembly compliance has little effect on weave and capsize speeds and, hence, on self-stability.

A parametric analysis was carried out in order to rank the influence of geometric, mass and compliance parameters on stability. Two stability indexes were applied: the difference between capsize and weave speeds (called here the self-stability range), and the area of the eigenvalue plots defined by the speed axis and the real parts of the weave and capsize eigenvalues when both are negative (self-stability area). Numerical results showed that the two indexes essentially give similar information, but that the self-stability area index includes more details than the self-stability range.

If a rigid bicycle is examined, the most influential design parameters are the position of the centre of mass in the longitudinal direction, trail, and front wheel radius. Forward displacement of the centre of mass and incremented trail increase stability; an increase in front wheel radius decreases stability.

When front assembly compliance is introduced in the set of bicycle parameters, numerical results show that the geometric and mass parameters do not change their effect on stability and that compliance has a very small destabilising effect.

References

Åström, K., J., Klein, R., E., Lennartsson, A., (2005) 'Bicycle dynamics and control', *IEEE Control System Magazine,* August 2005, 25(4), pp. 26-47.

Box G. E., Hunter W. G., and Hunter J. S., (2005) *Statistics for Experimenters: Design, Innovation, and Discovery, 2nd edn.*, John Wiley & Sons, Hoboken NJ.

Bulsink V.E., Doria A., Van De Belt D., Koopman B. (2015) 'The effect of tyre and rider properties on the stability of a bicycle', *Advances in Mechanical Engineering,* 7(12), pp.1-19.

Cossalter V. (2007) *Motorcycle Dynamics,* 2nd edn., Lulu.com.

Doria A., Tognazzo M., Cusimano G., Bulsink V., Cooke A., and Koopman B., (2013). 'Identification of the mechanical properties of bicycle tyres for modelling of bicycle dynamics', *Vehicle System Dynamics*, 51(3), 405-420.

Doria A and Tognazzo M. (2014) 'The influence of the dynamic response of the rider's body on the open loop stability of a bicycle', *Proceedings of the Institution of Mechanical Engineers, Part C: Journal of Mechanical Engineering Science*. 228(17), pp. 3116-3132.

Doria A., Taraborrelli L., Segliani L., (2015) 'The effect of front fork compliance on the stability of bicycles', P*roceedings of the ASME 2015 International Design Engineering Technical Conferences & Computers and Information in Engineering Conference IDETC/CIE 2015,* Vol. 3, Boston, Mass, USA.

Doria A., Taraborrelli L., (2016) 'The twist axis of frames with particular application to motorcycles', *Proc IMechE Part C: J Mechanical Engineering Science,* 230(17), pp. 3026–3039.

Doughty S., (1988) *Mechanics of Machines,* John Wiley & Sons, Hoboken NJ.

Ewins D.J. (2000) *Modal Testing: Theory and Practice, 2nd edn.* Research Studies Press, Baldock, United Kingdom.

Klinger F, Nusime J, Edelmann J and Plöchl M. (2014) 'Wobble of a racing bicycle with a rider hands on and hands off the handlebar', *Vehicle System Dynamics*, 52(sup1), pp. 51-68.

Kooijman J. D. G., Meijaard J. P., Papadopoulos J. M. Schwab A. L., (2011) 'A bicycle can be self-stable without gyroscopic and caster effects', *Science,* 332(6027), pp 339-342.

Limebeer, D. J. N., and Sharp, R. S. (2006), 'Bicycles, motorcycles, and models', *IEEE Control Systems, 26*(5), 34–61.

Magnani, G., Ceriani, N.M., Papadopoulos, J, (2013) 'On-road measurements of high speed bicycle shimmy, and comparison to structural resonance', *2013 IEEE International Conference on Mechatronics, ICM 2013,* Vicenza; Italy, pp 400-405.

Meijaard J.P, Papadopoulos J.M, Ruina A., Schwab A.L. (2007) 'Linearized dynamics equations for the balance and steer of a bicycle: a benchmark and review', *Proceedings of the Royal Society A: Mathematical, Physical and Engineering Science,* 463(2084), pp.1955-82.

Montgomery, D.C., (2008) *Design and Analysis of Experiments,* 3rd edn., John Wiley & Sons, Hoboken NJ.

Moore J., (2006) 'Low Speed Bicycle Stability: Effects of Geometric Parameters', *MAE 233*, August 2006.

Paceijka, H., (2006) *Tire and vehicle dynamics*, 2nd edn., Elsevier, Amsterdam, The Netherlands.

Plöchl, M., Edelmann, J., Angrosch, B., Ott, C. (2012) 'On the wobble mode of a bicycle'. V*ehicle System Dynamics*, *50*(3), 415–429.

Schwab A. L., Meijaard J. P., Kooijman J. D. G. (2012) 'Lateral dynamics of a bicycle with a passive rider model: stability and controllability', *Vehicle System Dynamics*, 50 (8), pp. 1209-1224.

Sharp, R. S. (2008). 'On the Stability and Control of the Bicycle', *Applied Mechanics Reviews*, 61(6), 60803.

Williams T., Kaul S., Dhingra A. (2016) 'Influence of frame stiffness and rider position on bike dynamics: analytical study', *Proceedings of ASME 2015 International Mechanical Engineering Congress and Exposition, IMECE 2015*; Houston, TX, USA, Vol. 4A-2015.

APPENDIX 1

The equations of the model with compliance represented by rotation β about the compliance axis are defined in matrix form in equation (A1).

$$[M]\begin{Bmatrix}\ddot{\varphi}\\ \ddot{\delta}\\ \ddot{\beta}\end{Bmatrix} + v[C_1]\begin{Bmatrix}\dot{\varphi}\\ \dot{\delta}\\ \dot{\beta}\end{Bmatrix} + \left[g[K_0] + v^2[K_2]\right]\begin{Bmatrix}\varphi\\ \delta\\ \beta\end{Bmatrix} + [C]\begin{Bmatrix}\dot{\varphi}\\ \dot{\delta}\\ \dot{\beta}\end{Bmatrix} + [K]\begin{Bmatrix}\varphi\\ \delta\\ \beta\end{Bmatrix} = \begin{Bmatrix}0\\0\\0\end{Bmatrix} \quad \textbf{(A1)}$$

Matrices $[M]$, $[C_1]$, $[K_0]$, $[K_2]$ have the same meaning as the corresponding matrices of the benchmark model (Meijaard 2007), but they have 3x3 dimensions and account for the additional terms due to structural compliance rotation. Mass matrix $[M]$ is defined in equation (A2).

$$[M] = \begin{bmatrix} M_{\varphi\varphi} & M_{\varphi\delta} & M_{\varphi\beta} \\ M_{\delta\varphi} & M_{\delta\delta} & M_{\delta\beta} \\ M_{\beta\varphi} & M_{\beta\delta} & M_{\beta\beta} \end{bmatrix} \quad \textbf{(A2)}$$

Terms $M_{\varphi\varphi}$, $M_{\varphi\delta}$, $M_{\delta\varphi}$ and $M_{\delta\delta}$ are defined according to Meijaard (2007). The new terms are defined in equations (A3) to (A7).

$$\mathrm{M_{\varphi\beta}} = \mathrm{I_{Fxx}}\cos\lambda - \mathrm{h_W m_F r_F} + \frac{1}{\mathrm{w}}[\mathrm{I_{Txz}}(\mathrm{h_W} + \mathrm{r_F}\cos\lambda)] \quad \textbf{(A3)}$$

$$\begin{aligned} M_{\delta\beta} = \quad & -h_W m_F (u_W + c\cos\lambda) \\ & + \frac{1}{w}[I_{A\lambda z} h_W + I_{A\lambda z} r_F \cos\lambda - I_{Fxx}\, c\cos\lambda\sin\lambda] \\ & + \frac{1}{w^2}[I_{Tzz}\, c\cos\lambda\,(h_W + r_F\cos\lambda)] \end{aligned} \quad \textbf{(A4)}$$

$$\mathrm{M}_{\beta\varphi} = \mathrm{M}_{\varphi\beta} \quad \textbf{(A5)}$$

$$\mathrm{M}_{\beta\delta} = \mathrm{M}_{\delta\beta} \quad \textbf{(A6)}$$

$$\begin{aligned} M_{\beta\beta} = \quad & I_{Fxx} - h_W^2 m_F - 2h_W m_F r_F \cos\lambda \\ & -\frac{1}{w}[2I_{Fxx} \sin\lambda\,(h_W + r_F \cos\lambda)] \\ & +\frac{1}{w^2}[I_{Tzz}(h_W + r_F \cos\lambda)^2] \end{aligned} \quad \textbf{(A7)}$$

Damping matrix $[C_1]$ is defined in equation (A8).

$$[C_1] = \begin{bmatrix} C_{1\varphi\varphi} & C_{1\varphi\delta} & C_{1\varphi\beta} \\ C_{1\delta\varphi} & C_{1\delta\delta} & C_{1\delta\beta} \\ C_{1\beta\varphi} & C_{1\beta\delta} & C_{1\beta\beta} \end{bmatrix} \quad \textbf{(A8)}$$

Terms $C_{1\varphi\varphi}$, $C_{1\varphi\delta}$, $C_{1\delta\varphi}$ and $C_{1\delta\delta}$ are defined according to Meijaard (2007). The new terms are defined in equations (A9) to (A13).

$$\begin{aligned} C_{1\varphi\beta} = \quad & -S_F \sin\lambda \\ & -\frac{1}{w}[I_{Txz} \sin\lambda - S_T h_W + h_W m_T z_T - S_T r_F \cos\lambda + m_T r_F z_T \cos\lambda] \end{aligned} \quad \textbf{(A9)}$$

$$\begin{aligned} C_{1\delta\beta} = \quad & -S_F \\ & +\frac{1}{w}[h_W m_A u_A - S_F\, c \cos^2\lambda - I_{A\lambda z} \sin\lambda + S_F h_W \sin\lambda + m_A r_F u_A \cos\lambda + S_F r_F \cos\lambda \sin\lambda] \\ & +\frac{1}{w^2}[c \cos\lambda\,(h_W m_T x_T - I_{Tzz} \sin\lambda + m_T r_F x_T \cos\lambda)] \end{aligned} \quad \textbf{(A10)}$$

$$C_{1\beta\varphi} = S_F \sin\lambda - \frac{1}{w}[S_T(h_W + r_F \cos\lambda)] \quad \textbf{(A11)}$$

$$C_{1\beta\delta} = S_F - h_W m_F \cos\lambda - \frac{1}{w}[I_{Fxx}\cos\lambda\sin\lambda - S_F\, c\cos^2\lambda + S_F h_W \sin\lambda + c\, h_W m_F \cos\lambda + S_F r_F \cos\lambda\sin\lambda] + \frac{1}{w^2}[\cos\lambda\,(I_{Tzz} + c\, m_T x_T)(h_W + r_F\cos\lambda)] \quad \textbf{(A12)}$$

$$C_{1\beta\beta} = h_W m_F \sin\lambda - \frac{1}{w}[m_F h_W^2 + m_F r_F \cos\lambda\, h_W - I_{Fxx}\sin^2\lambda] + \frac{1}{w^2}[(h_W + r_F\cos\lambda)(h_W m_T x_T - I_{Tzz}\sin\lambda + m_T r_F x_T\cos\lambda)] \quad \textbf{(A13)}$$

Stiffness matrix $[K_0]$ is defined in equation (A14).

$$[K_0] = \begin{bmatrix} K_{0\varphi\varphi} & K_{0\varphi\delta} & K_{0\varphi\beta} \\ K_{0\delta\varphi} & K_{0\delta\delta} & K_{0\delta\beta} \\ K_{0\beta\varphi} & K_{0\beta\delta} & K_{0\beta\beta} \end{bmatrix} \quad \textbf{(A14)}$$

Terms $K_{0\varphi\varphi}$, $K_{0\varphi\delta}$, $K_{0\delta\varphi}$ and $K_{0\delta\delta}$ are defined according to Meijaard (2007). The new terms are defined in equations (A16) to (A20). The common term R_W is introduced in equation (A15) for the above-mentioned stiffness terms.

$$R_w = -m_F h_W + (h_W + r_F\cos\lambda)\frac{m_T x_T}{w} \quad \textbf{(A15)}$$

$$K_{0\varphi\beta} = -R_w \quad \textbf{(A16)}$$

$$K_{0\delta\beta} = -R_w \sin\lambda \quad \textbf{(A17)}$$

$$K_{0\beta\varphi} = K_{0\varphi\beta} \quad \textbf{(A18)}$$

$$K_{0\beta\delta} = K_{0\delta\beta} \quad \textbf{(A19)}$$

$$K_{0\beta\beta} = -R_w \cos\lambda \quad \textbf{(A20)}$$

Stiffness matrix $[K_2]$ is defined in equation (A21).

$$[K_2] = \begin{bmatrix} K_{2\varphi\varphi} & K_{2\varphi\delta} & K_{2\varphi\beta} \\ K_{2\delta\varphi} & K_{2\delta\delta} & K_{2\delta\beta} \\ K_{2\beta\varphi} & K_{2\beta\delta} & K_{2\beta\beta} \end{bmatrix} \quad \textbf{(A21)}$$

Terms $K_{2\varphi\varphi}$, $K_{2\varphi\delta}$, $K_{2\delta\varphi}$ and $K_{2\delta\delta}$ are defined according to Meijaard (2007). The new terms are defined in equations (A22) to (A26).

$$K_{2\varphi\beta} = -\frac{1}{w}[\sin\lambda\,(S_T - m_T z_T)] \quad \textbf{(A22)}$$

$$K_{2\delta\beta} = -\tfrac{1}{w}[\sin\lambda\,(m_A u_A + S_F \sin\lambda)] - \tfrac{1}{w^2}[c m_T x_T \cos\lambda \sin\lambda] \quad \textbf{(A23)}$$

$$K_{2\beta\varphi} = 0 \quad \textbf{(A24)}$$

$$K_{2\beta\delta} = -\tfrac{1}{w}[\cos\lambda\,(h_W m_F - S_F \cos\lambda)] + \tfrac{1}{w^2}[m_T x_T \cos\lambda\,(h_W + r_F \cos\lambda)] \quad \textbf{(A25)}$$

$$K_{2\beta\beta} = \tfrac{1}{w}[\sin\lambda\,(h_W m_F - S_F \cos\lambda)] - \tfrac{1}{w^2}[m_T x_T \sin\lambda\,(h_W + r_F \cos\lambda)] \quad \textbf{(A26)}$$

Matrices $[C]$, $[K]$ are 'true' damping and stiffness matrices and take into account the stiffness and damping properties of structural compliance. They are shown in equations (A27) and (A28).

$$[C] = \begin{bmatrix} 0 & 0 & 0 \\ 0 & 0 & 0 \\ 0 & 0 & c_\beta \end{bmatrix} \quad \textbf{(A27)}$$

$$[K] = \begin{bmatrix} 0 & 0 & 0 \\ 0 & 0 & 0 \\ 0 & 0 & k_\beta \end{bmatrix} \quad \textbf{(A28)}$$

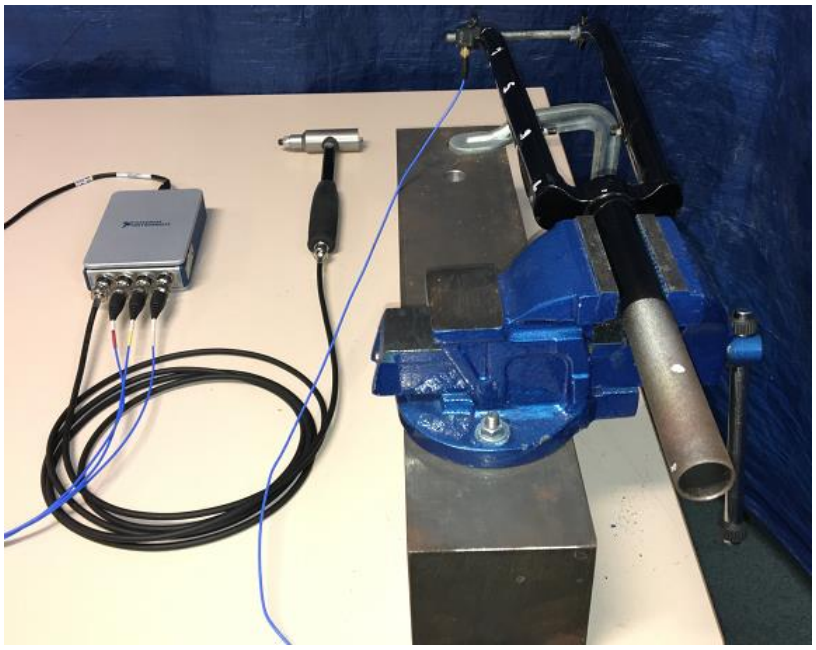

Figure 1. Front fork fixed in clamp.

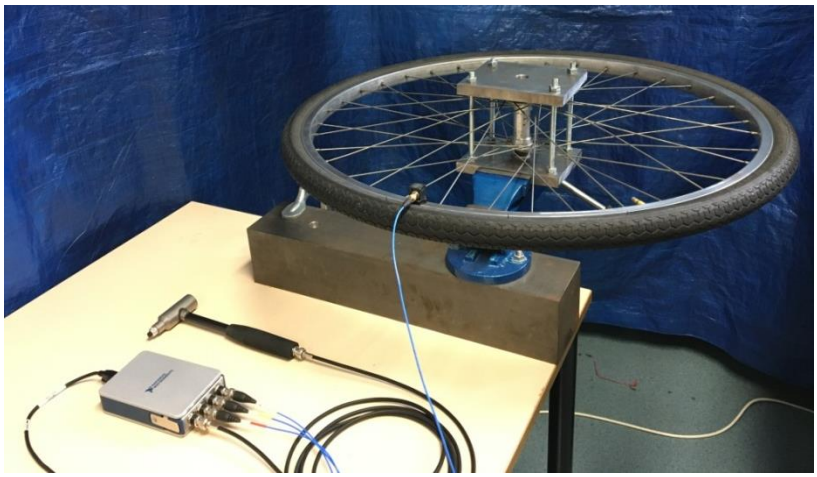

Figure 2. Wheel mounted with wheel hub attached at both ends.

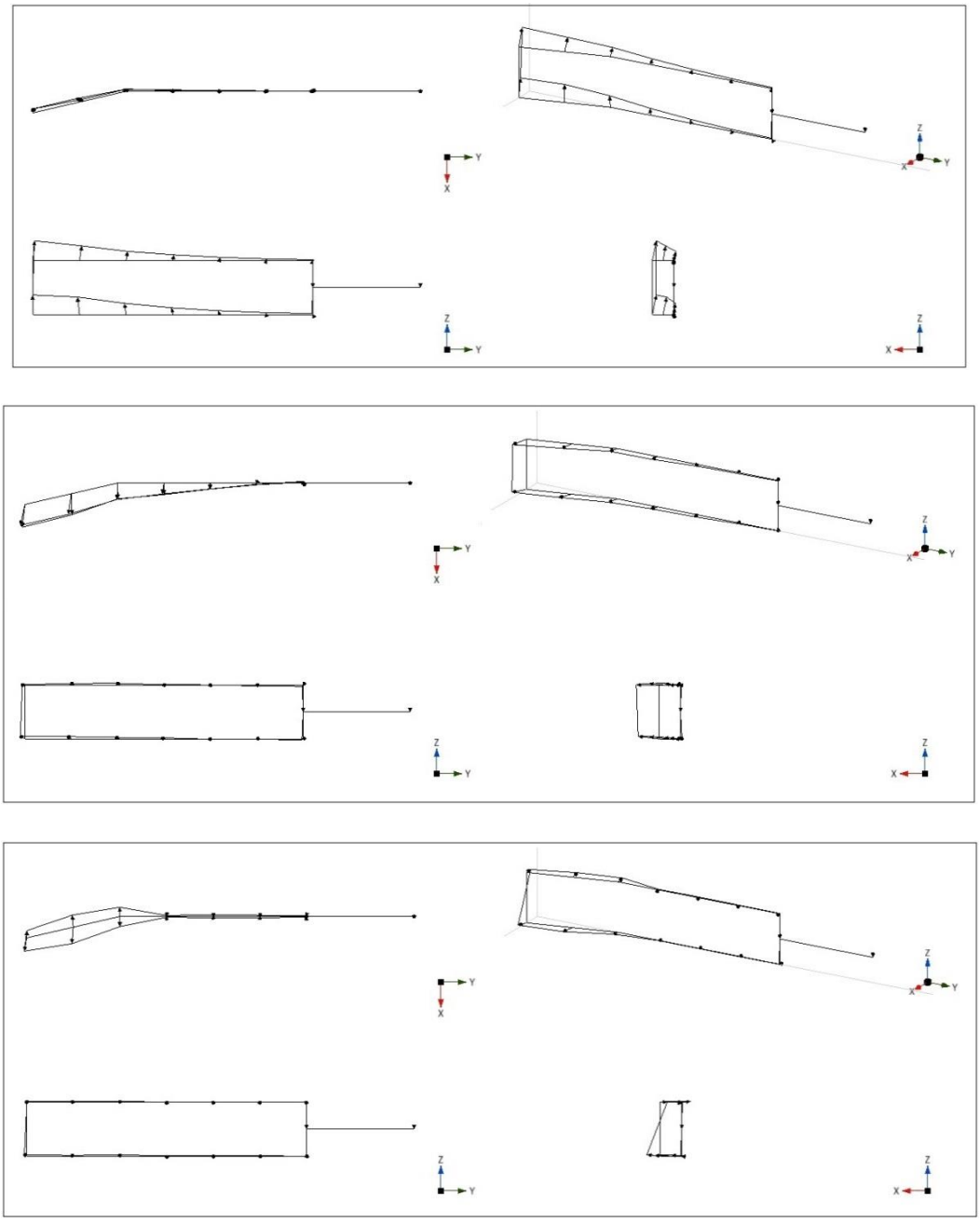

Figure 3. Modes of fork alone (from top: lateral, longitudinal and torsional modes).

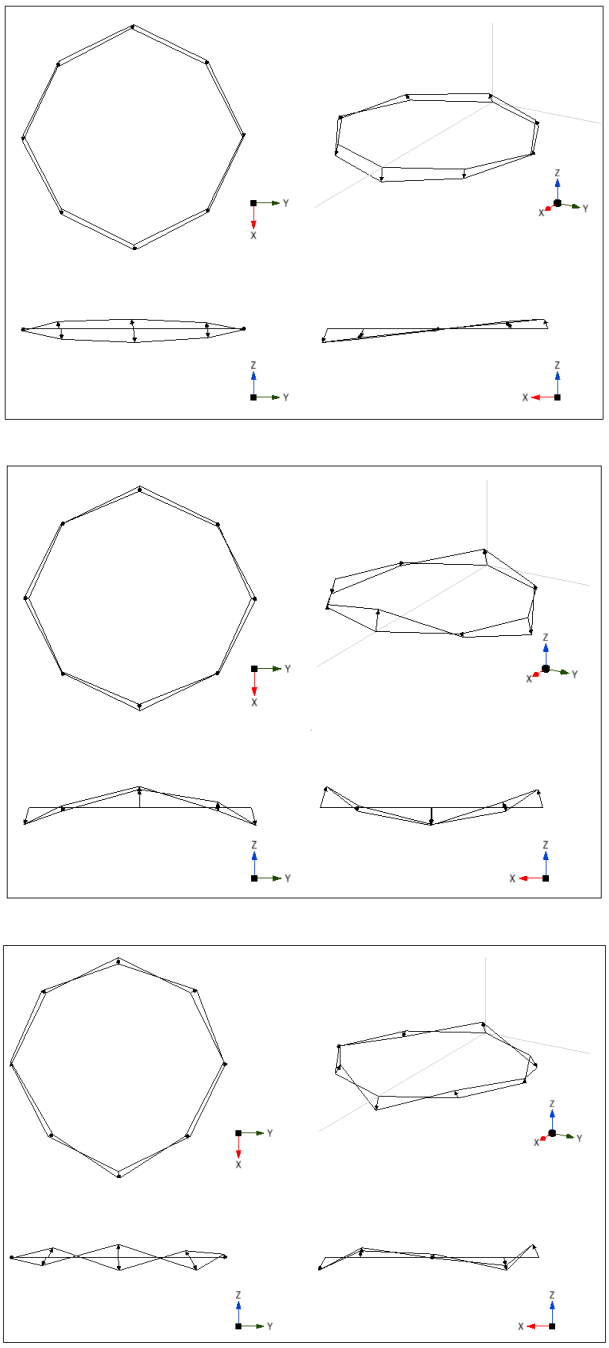

Figure 4. Modes of wheel alone (from top: diametric, C-shaped and S-shaped modes).

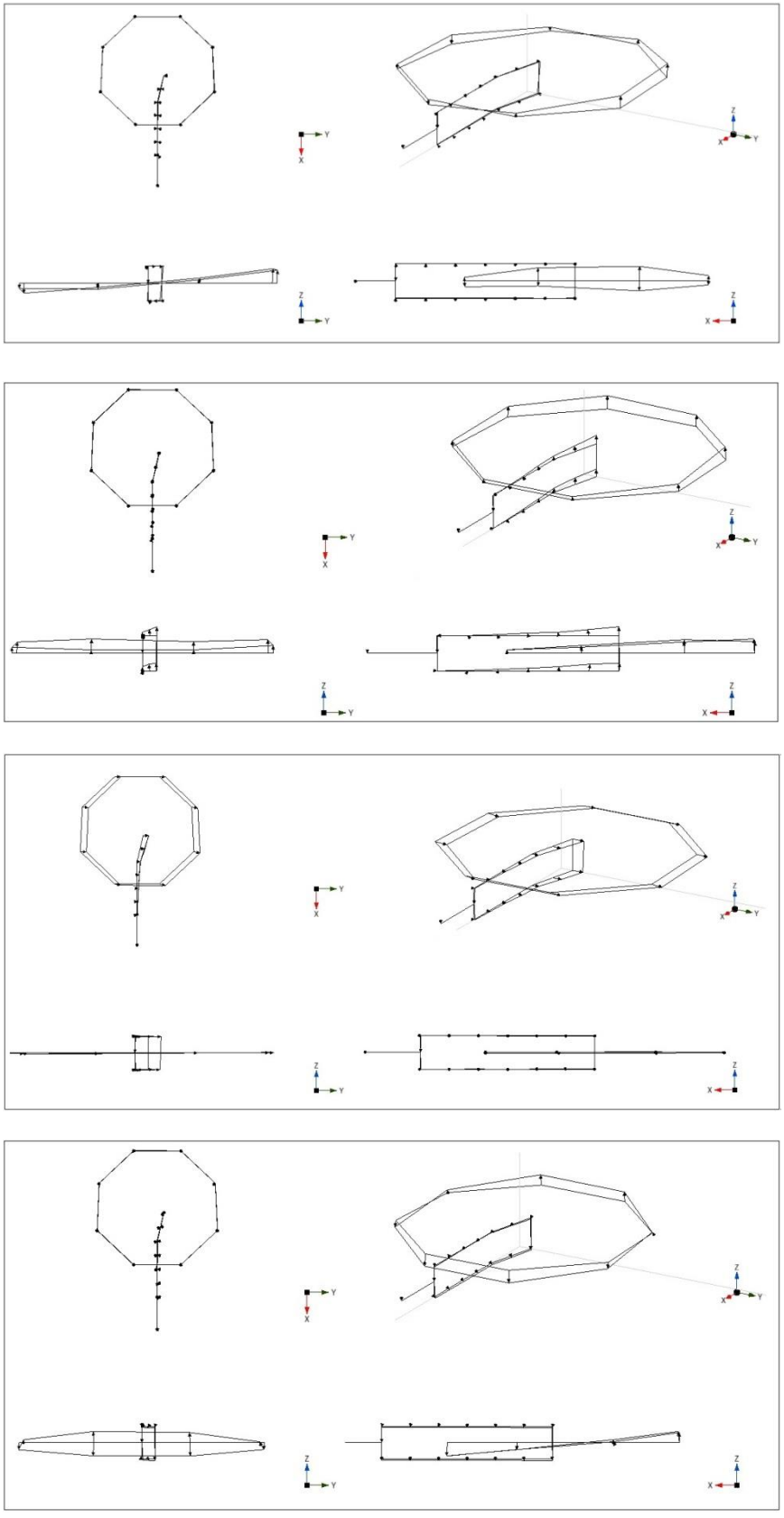

Figure 5. Modes of front assembly. From top: torsional, lateral, longitudinal and second lateral mode.

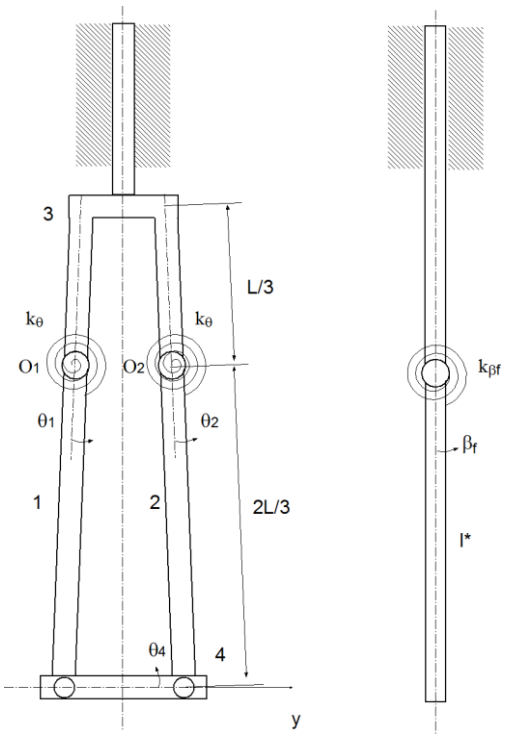

Figure 6. Fork model for lumped stiffness calculation.

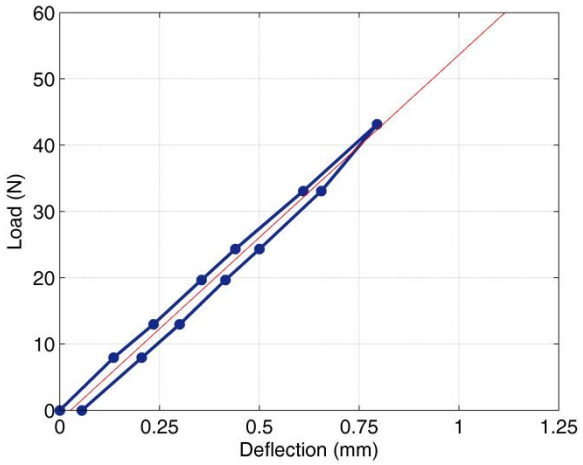

Figure 7. Static stiffness curve of fork in lateral direction.

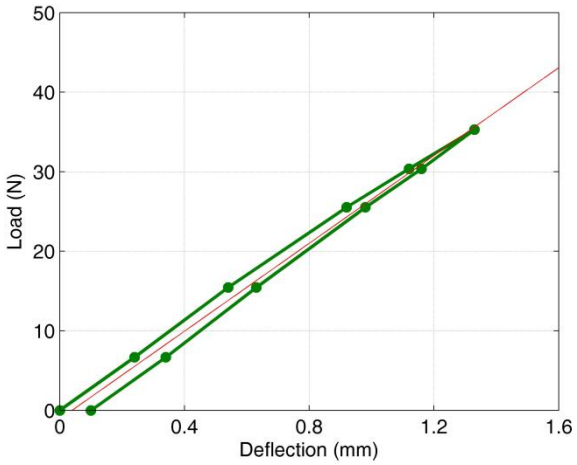

Figure 8. Static stiffness of wheel about diameter.

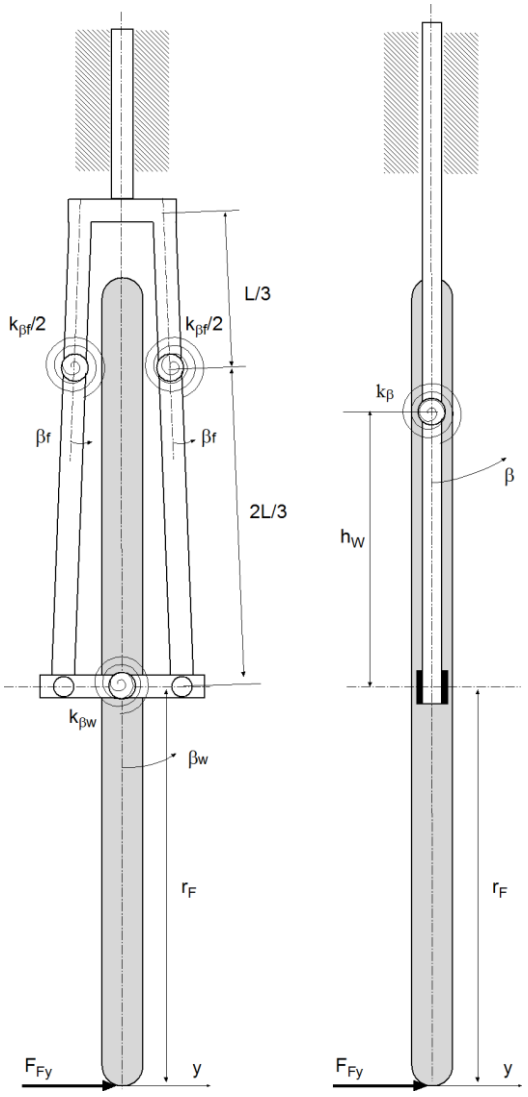

Figure 9. Lumped element model of front assembly.

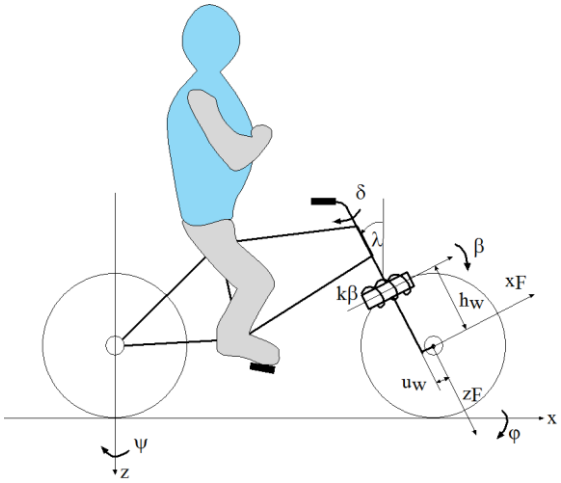

Figure 10. Bicycle model with bending compliance of front assembly.

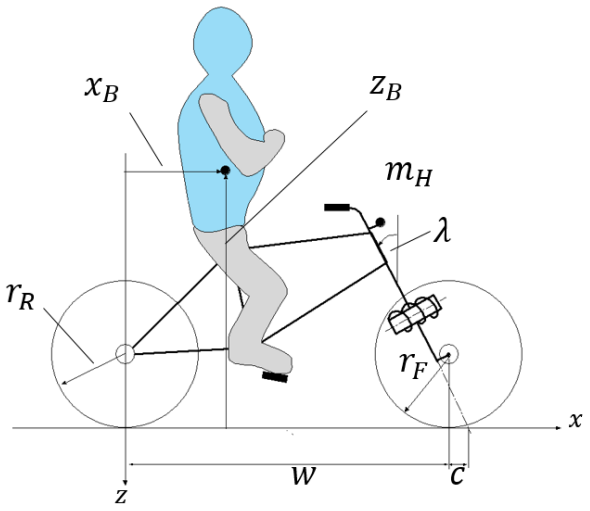

Figure 11. Bicycle parameters.

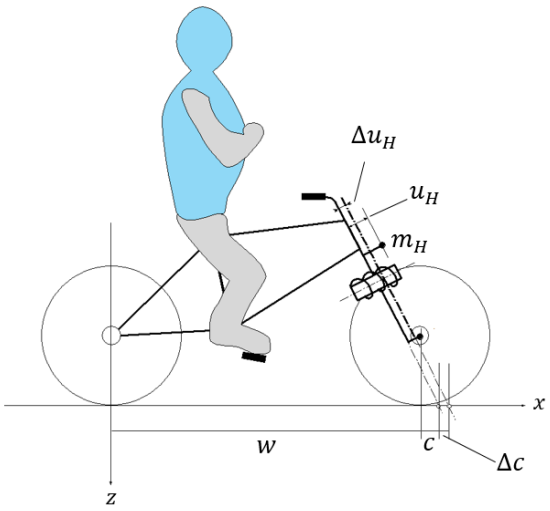

Figure 12. Effect of c on distance between m_H and steer axis.

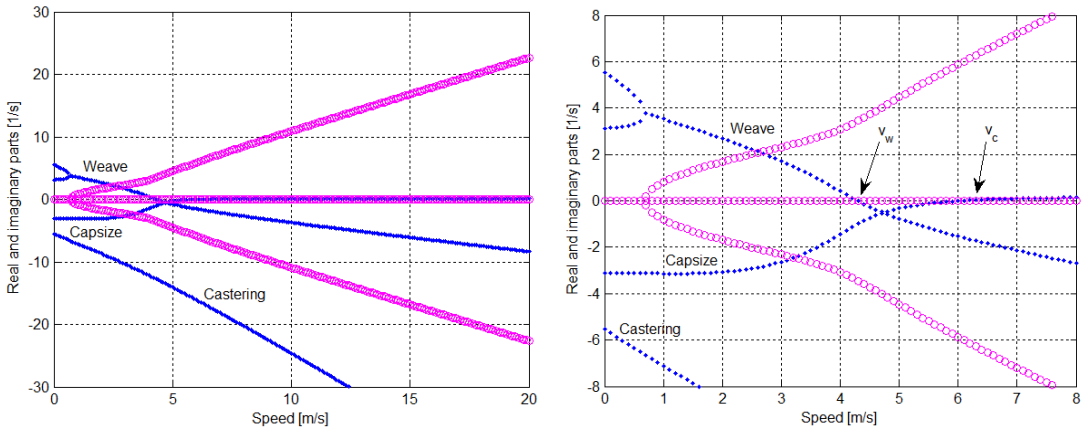

Figure 13. Eigenvalues of benchmark bicycle with rigid front assembly.

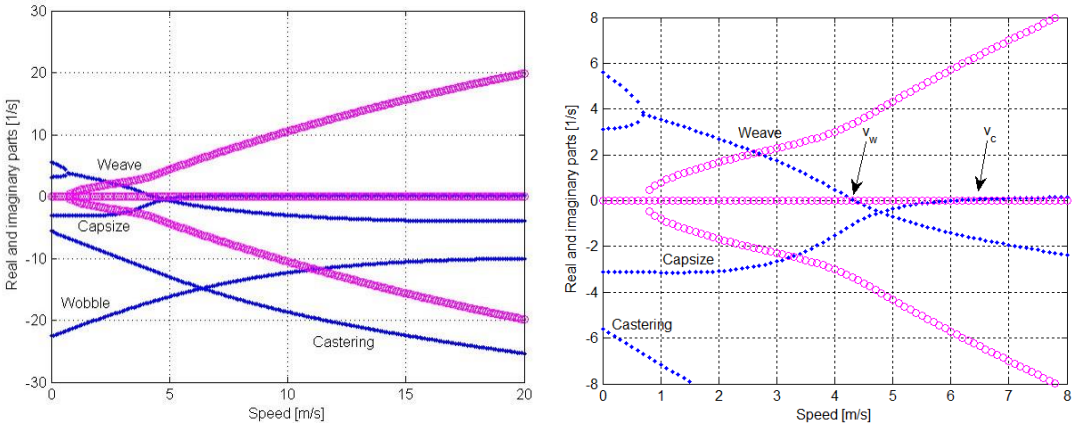

Figure 14. Eigenvalues of the benchmark bicycle with compliant wheel.

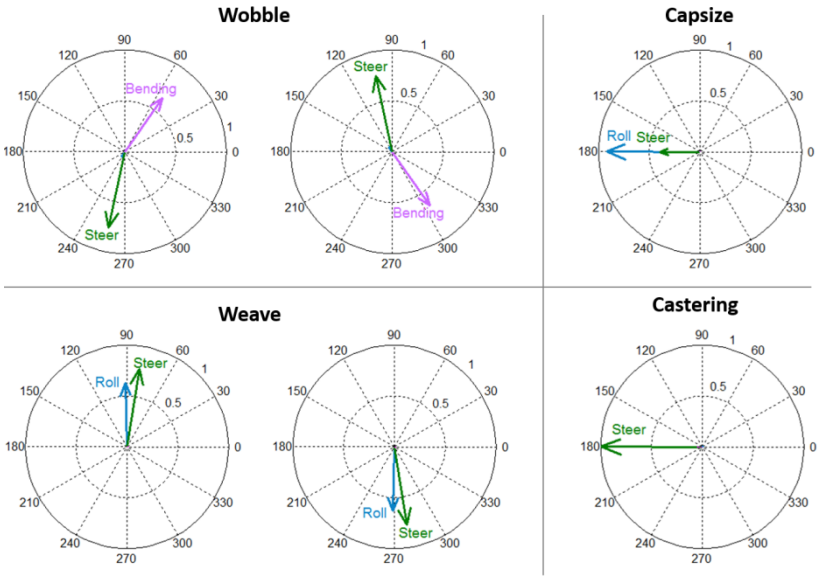

Figure 15. Modes of vibration of benchmark bicycle with compliant wheel at 5 m/s. Shapes are shown by vector diagrams. Arrows: amplitude and phase of modal components.

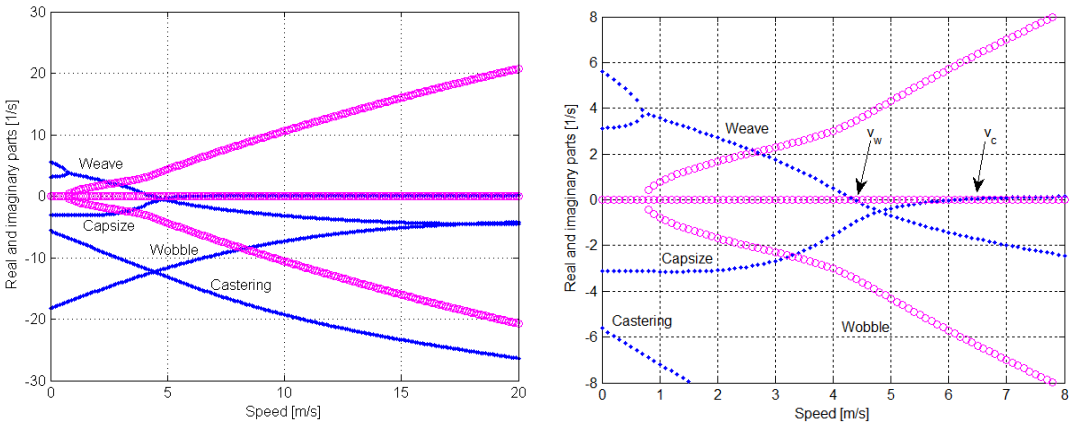

Figure 16. Eigenvalues of benchmark bicycle with compliant front assembly.

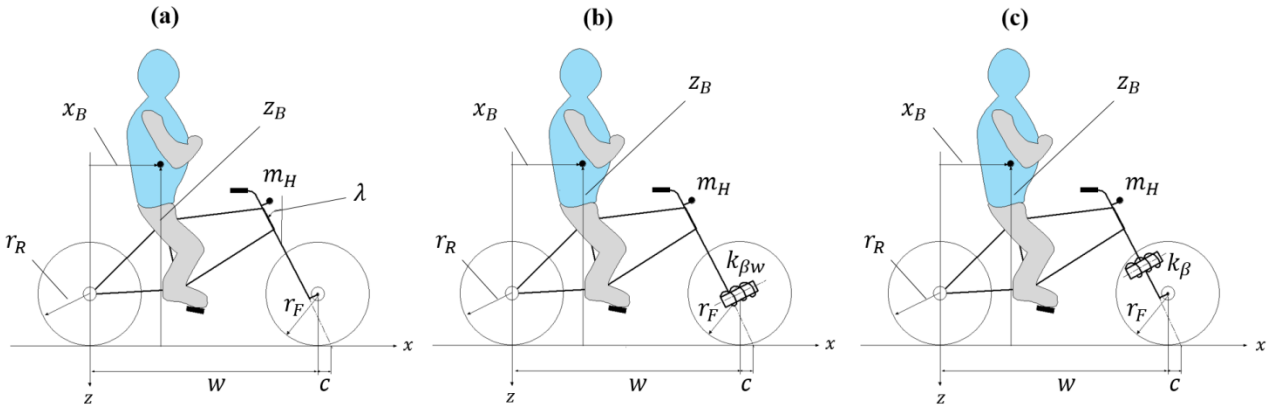

Figure 17. (a) Rigid bicycle. (b) Bicycle with wheel compliance. (c) Bicycle with front assembly compliance.

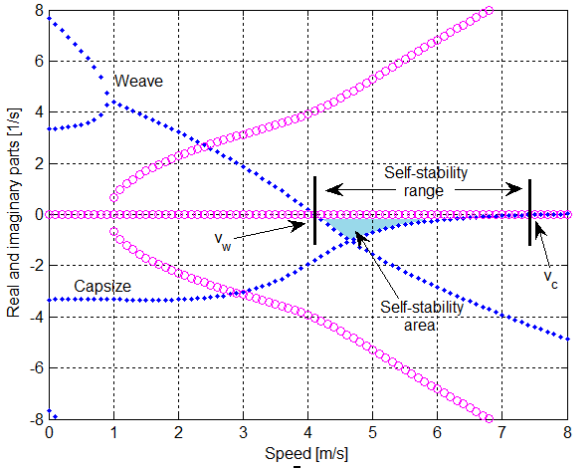

Figure 18. Definition of stability indexes.

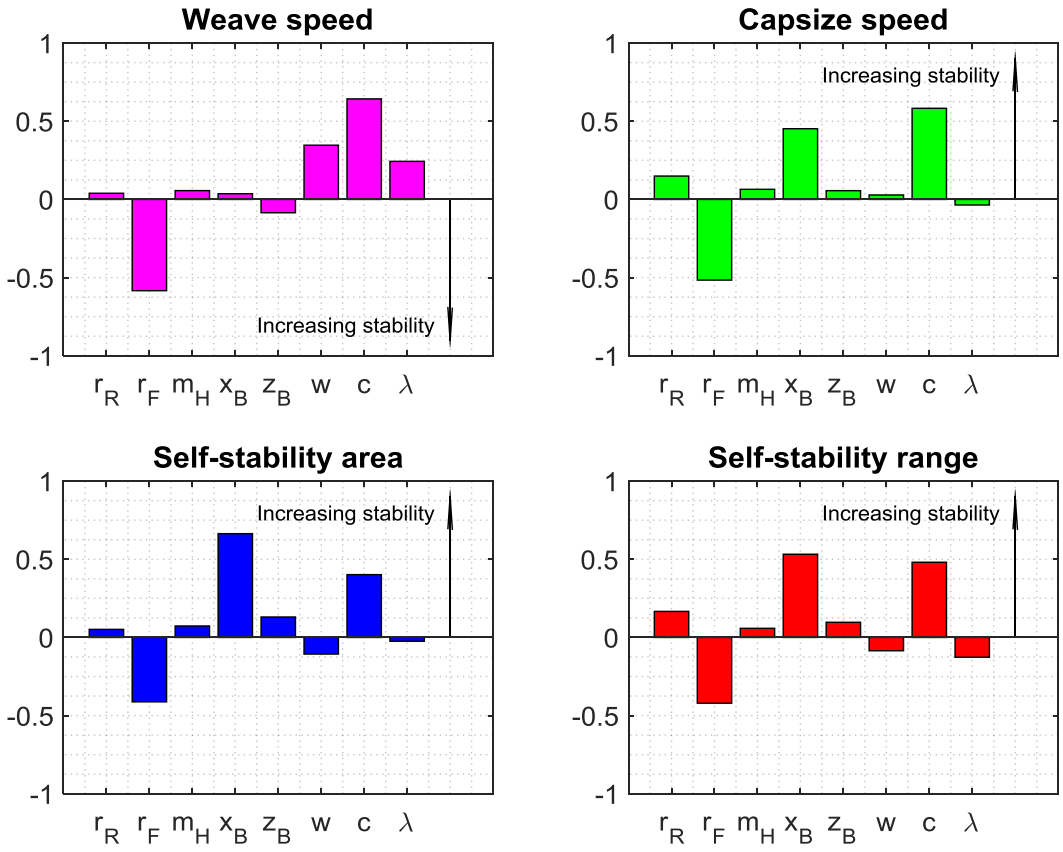

Figure 19. Results of correlation analysis results, rigid bicycle.

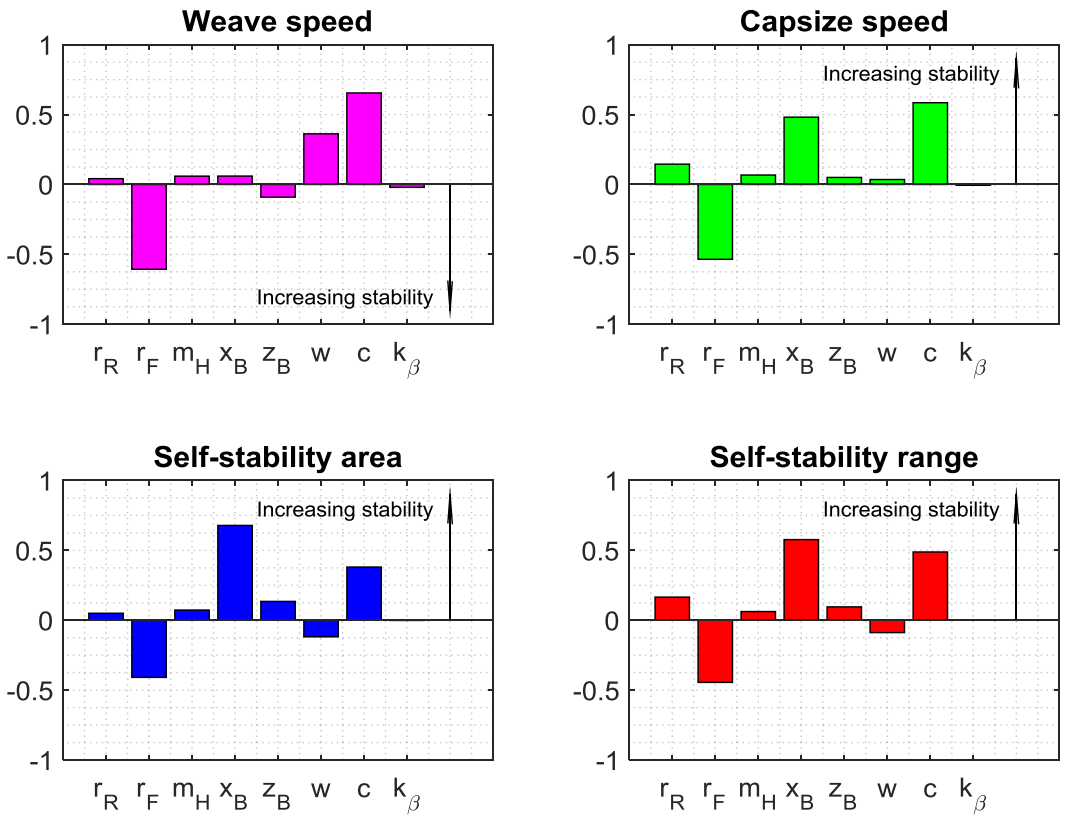

Figure 20. Correlation analysis results, bicycle with compliant wheel.

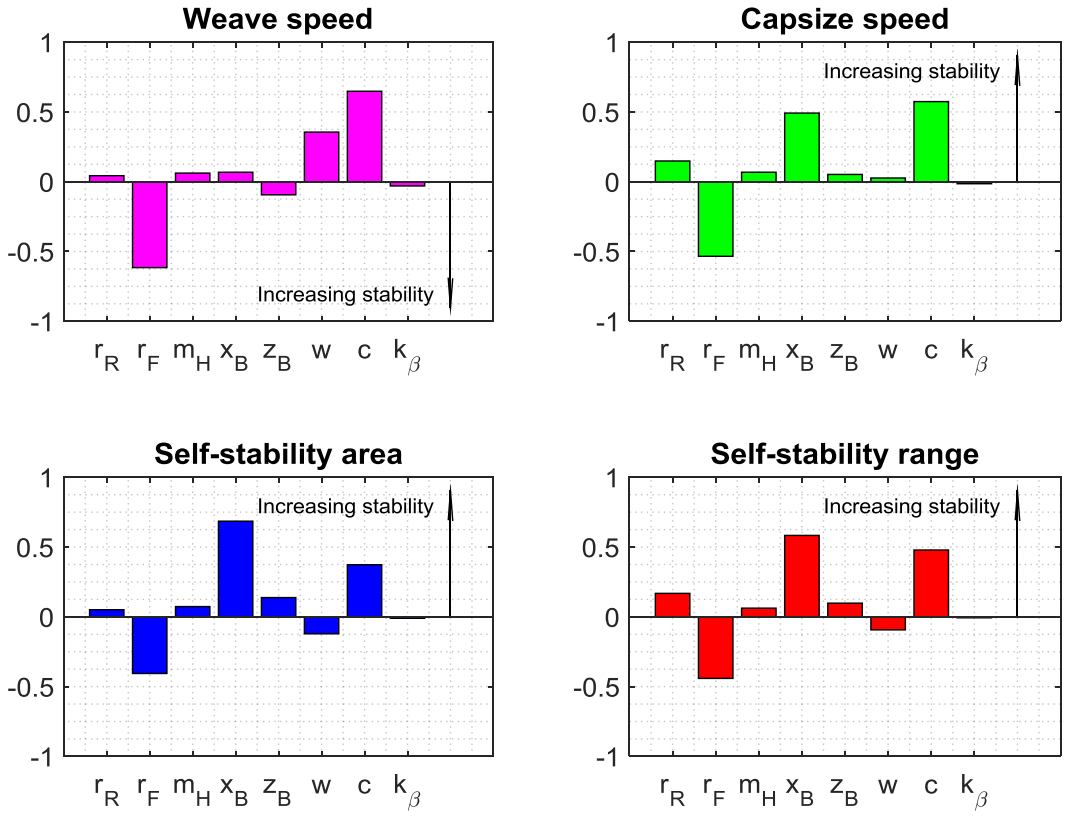

Figure 21. Correlation analysis results, bicycle with compliant front assembly.

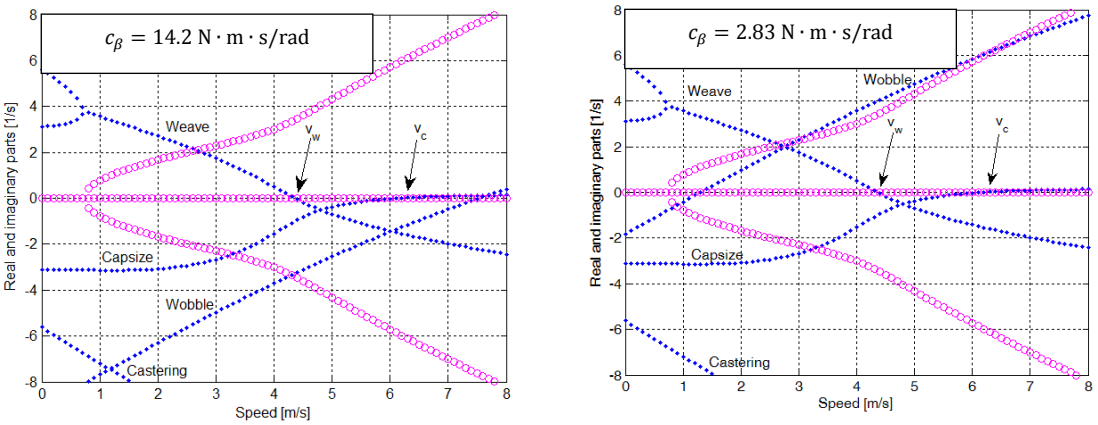

Figure 22. Eigenvalues of bicycle with compliant front assembly and decreasing values of damping.

Table 2. Modal properties of fork alone.

f (Hz)	ζ (%)	Description
73.94	1.31	Lateral bending
87.38	2.67	Longitudinal bending
196.3	0.391	Torsion

Table 2. Modal properties of wheel alone.

f (Hz)	ζ (%)	Description
27.75	1.607	Diametric
99.66	0.8707	C-shaped
148.8	1.292	S-shaped

Table 3. Modal properties of fork with wheel.

f (Hz)	ζ (%)	Description
17.7	0.181	Torsional
24.99	0.552	Lateral bending
26.86	0.586	Longitudinal bending
53.38	1.041	Wheel diametric with fork in opposition

Table 4. Design parameters.

Parameter	Nominal value	Low level	High level	Standard deviation / Nominal value
Rear wheel radius r_R	0.305 m (12 in)	0.254 m (10 in)	0.356 m (14 in)	0.167
Front wheel radius r_F	0.337 m (13.25 in)	0.305 m (12 in)	0.368 m (14.5 in)	0.0943
Handlebar and fork mass m_H	4 kg	3 kg	5 kg	0.25
Rear body and frame horizontal coordinate X_B	0.3 m	0.2 m	0.4 m	0.333
Rear body and frame vertical coordinate Z_B	-0.9 m	-0.75 m	-1.05 m	0.167
Wheelbase w	1.02 m	0.80 m	1.24 m	0.216
Trail c	0.08 m	0.05 m	0.11 m	0.375
Caster angle λ	18° [π/10 rad]	15° [π/12 rad]	21° [7 π/60 rad]	0.167
Wheel stiffness $k_{\beta w}$	2888 N · m/rad	2166 N · m/rad	3610 N · m/rad	0.25
Assembly stiffness k_β	4018 N · m/rad	3013 N · m/rad	5022 N · m/rad	0.25

Table 5. Self-stability ranges for various model extensions.

Model	v_w [m/s]	v_c [m/s]	Stability range [m/s]	Reference
WCBM	4.292	6.024	1.732	Meijaard 2007
With wheel compliance	4.344	6.061	1.717	Figure 14
With front assembly compliance	4.358	6.114	1.756	Figure 15
With linear tyre model	4.1*	5.4*	1.3*	Sharp 2008
With rider torsion compliance	4.291	6.024	1.733	Doria 2014
With rider leaning sideways	4.237	6.018	1.781	Doria 2014

*Data obtained from plot in which only two digits are significant.